

mm

APPENDIX A

Statistical Approaches to Ozone Trend Detection

Panel Members

P. Bloomfield, Chair

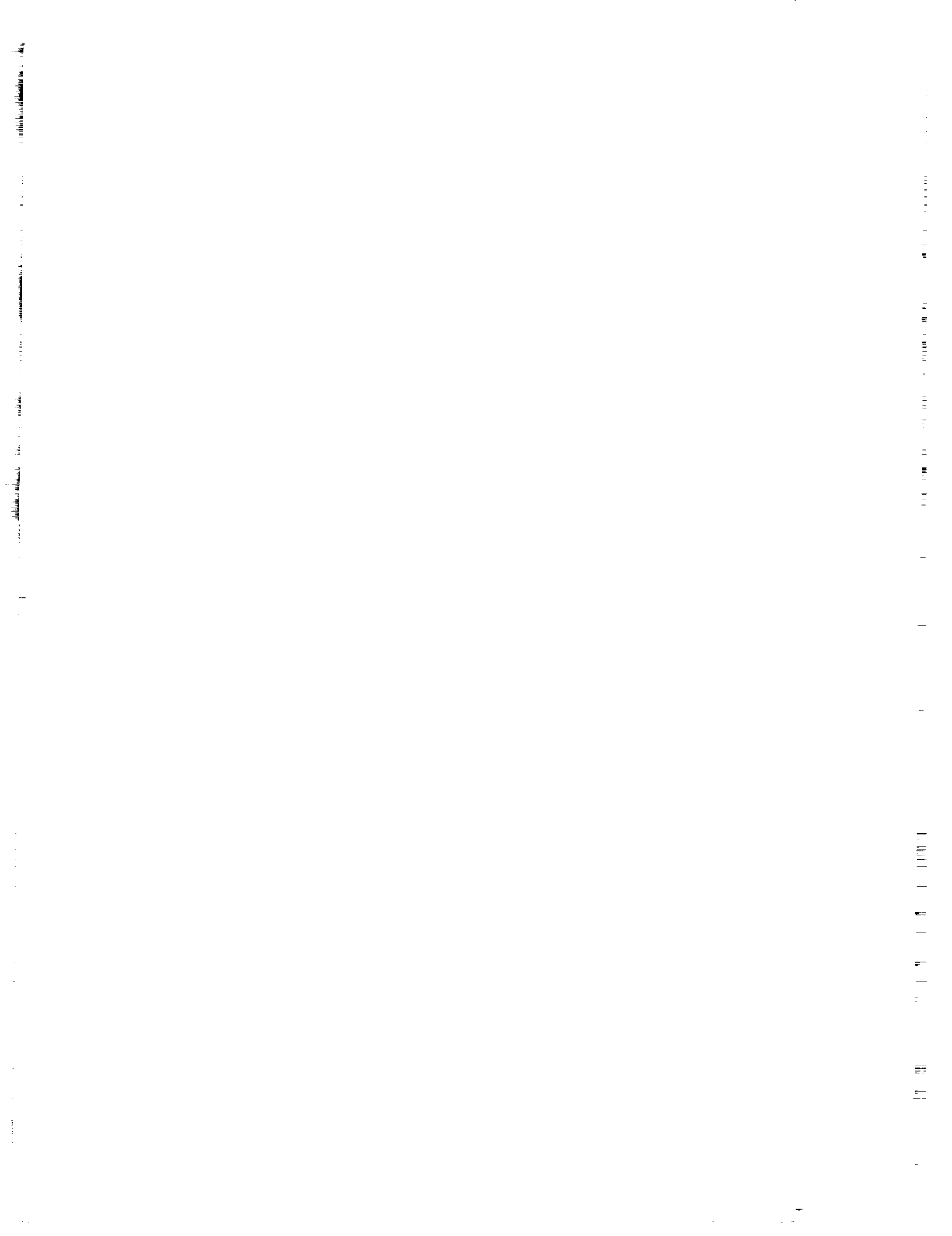
D. R. Brillinger

D. W. Nychka

R. S. Stolarski

WC 999967

✓

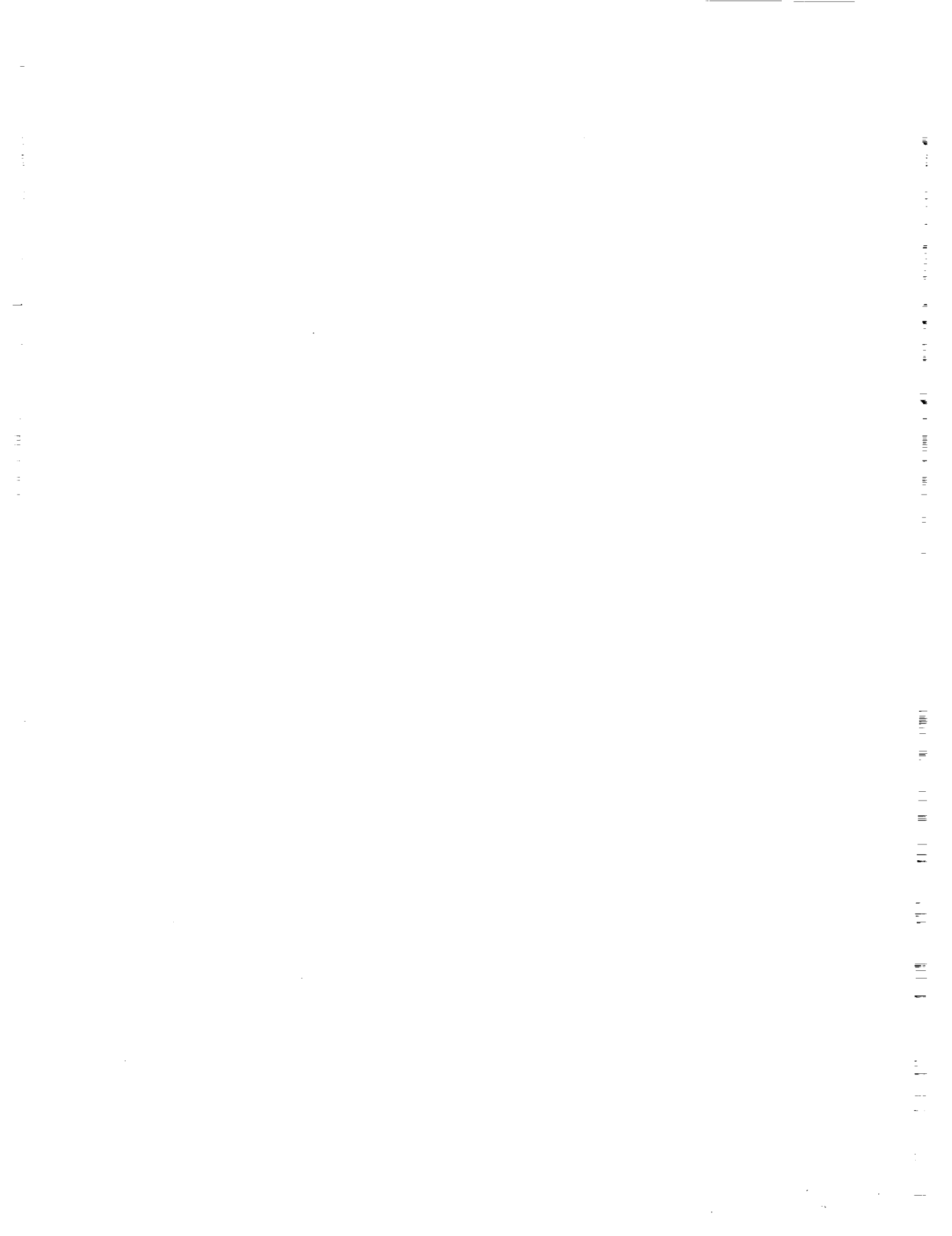


Appendix A

Statistical Approaches to Ozone Trend Detection

Contents

1.0	CURRENT STATUS OF STATISTICAL ANALYSES	755
1.1	Ground-Based Total Column Ozone	755
1.2	Ground-Based Ozone Profiles (Umkehr)	758
1.3	Satellite Data	759
2.0	TEMPORAL AND SPATIAL CORRELATION	760
2.1	Least-Squares Estimates	760
2.2	Interpretation of Standard Error	761
2.3	Limitations of the Model	761
2.4	An Elementary Model for Temporal Correlation	764
2.5	More General Temporal Models	766
2.6	Spatial Correlation	767
3.0	SEASONALITY IN OZONE DATA	768
3.1	Seasonal Structure in the Mean	769
3.2	Seasonal Structure in the Trend	770
3.3	Seasonal Structure in the Correlations	771
4.0	SUMMARY	772



1.0 CURRENT STATUS OF STATISTICAL ANALYSES

The statistical analyses compiled by Reinsel, Tiao, and their coworkers provide the most comprehensive work on trend direction. This group's efforts represent a long-term involvement with ozone data. Their methods have been published in peer-reviewed statistical journals (Reinsel and Tiao, 1987), and previous discrepancies with other approaches have been reconciled (Hill et al., 1986). Stemming from this statistical work are some recent analyses concerning seasonal trends in total ozone for some of the stations in the Dobson network, reported in Chapter 4 of this report. There is a substantial amount of analysis of ozone measurements in the meteorological literature, such as the work by Angell and Korshover (1983b). However, because such studies do not adequately adjust for the short-term correlation in ozone over time, their results are of limited value for drawing conclusions about trends in ozone. For these reasons, this review will concentrate on the methods developed by Reinsel and Tiao.

1.1 Ground-Based Total Column Ozone

The most complete statistical analysis of ground-based ozone measurements is by Reinsel et al. (1987). Based on the measurements of a global network of 36 Dobson spectrophotometers, an average trend of -0.026 ± 0.092 percent per year¹ was estimated over the period 1970–1984². Perhaps the most important aspect of interpreting these results is to distinguish between the average trend associated with these 36 locations and a global trend in total column ozone. They need not be the same. Although satellite data (see Section 1.3) suggest that trend analysis based on the Dobson network is representative of a global trend, more investigation in this area is needed. At present it is uncertain how to extrapolate the average trend among the Dobson network to a global trend for the entire atmosphere.

In order to discuss the assumptions that lead to the average trend cited above and to compare this analysis with other work, it is helpful to describe the statistical model used by Reinsel and Tiao. This model accounts for several factors that influence trend detection: the seasonal behavior of ozone, the relationship of ozone with the solar activity, and short-term auto-correlation within the ozone series. Let Y_t represent the monthly average total ozone recorded from a particular Dobson station. This observation is assumed to have the following decomposition:

$$Y_t = \mu + S_t + \omega X_t + \gamma Z_t + N_t. \quad (1)$$

In the above expression, μ represents a mean level, S_t is a seasonal component, X_t is a ramp function modeling a linear trend in ozone beginning in 1970, Z_t is the monthly average of 10.7 cm solar flux (or a smoothed version of it), and, finally, N_t is a random variable representing the short-term variation in ozone. The parameter ω represents the trend in ozone. Using this statistical model and some assumptions on the short-term variation, it is possible to estimate ω and also derive a measure of the uncertainty in this estimate.

It is well accepted that the monthly fluctuations in ozone are not independent of one another and tend to be positively correlated. One way of accounting for this behavior is to assume that

¹ In this appendix all \pm limits correspond to 95 percent confidence intervals.

² This trend estimate has been updated to -0.05 ± 0.07 percent per year during the longer period of 1970–1986 for a network of 43 Dobson stations (Reinsel, 1988, personal communication).

STATISTICS

$\{N_i\}$ is approximated by an autoregressive time series (see Sections 2.4, 2.5, and 3.3 for more detail). Another approach using spectral analysis is given by Bloomfield et al. (1983). This part of the statistical model is necessary in order to obtain reliable measures of uncertainty for the trend estimate. Unfortunately, the trend estimates reported by Angell and Korshover (1983b) and Heath (1986) based on ordinary least-squares are of unknown accuracy because the standard errors (SE's) do not allow for autocorrelation. This issue is discussed at length in Section 2.

The other components in this model are also related to the estimate of ω . Modeling seasonality of the ozone measurements reduces the variance in the data and thus improves the accuracy of the trend estimate. The inclusion of the solar flux reduces bias in the estimate of ω by distinguishing behavior in ozone due to solar cycle from other long-term trends.

The statistical model described above is used by Reinsel and Tiao to obtain trend estimates for each station. Using a random effects model to describe variation between stations, these estimates are combined to yield an average trend for the Dobson network. In order to be able to interpret this estimated average trend, this random effects model will be briefly described. The 36 stations can be divided into seven geographic regions (see Table 1, from Hill et al., 1986). Let $\omega_{i,j}$ denote the actual trend in total ozone for the i th station in the j th region. This trend is assumed to satisfy the equation

$$\omega_{i,j} = \omega + \alpha_j + \beta_{i,j}$$

where ω is the actual "global" trend in ozone, α_j is a zero mean random variable that reflects the variability in trends between different regions, and $\beta_{i,j}$ is a zero mean random variable that reflects the variability of trends within a region. It should be noted that the term $\beta_{i,j}$ not only represents variability due to meteorological effects but also accounts for spurious trends such as calibration problems for particular stations. With this decomposition, the estimated trend for a particular station can be expressed as

$$\hat{\omega}_{i,j} = \omega + \alpha_j + \beta_{i,j} + E_{i,j}$$

where $E_{i,j}$ is the error in the trend estimate due to the variability of the ozone within a station's record.

This "random effects" model can be used to derive an estimate for ω that is a weighted average of the individual trend estimates; a standard error for this estimate can also be calculated. This approach for combining individual trend estimates has an advantage over a simple average because it adjusts for correlation among stations within the same region. The spatial correlation implied by this model, however, has a simple structure that may not be a good approximation of the ozone field. It assumes that all stations within a region are equally correlated while stations in different regions are independent. A more serious problem is interpreting the parameter ω . Although Reinsel et al. (1987) refer to ω as a global trend in ozone, this is an assumption and is not implied by the random effects model. A more precise definition of ω is that it represents the component of trend in total ozone that is common to all the stations used in the analysis.

An alternative to the time domain approach of Reinsel and Tiao can be found in Bloomfield et al. (1983). Rather than using a random effects model to combine estimated trends, a similar model is used to construct an average ozone series. The parameter ω is then estimated from the

Fourier transform of this single series. This frequency domain analysis has the advantage that less need be assumed about the structure of the short- and long-term variation in ozone. One

Table 1. Dobson Network Used in Total Ozone Trend Analysis

Region	Station	Location	Data Period
North America	Resolute, Canada	75°N, 95°W	Jan. 1958–Dec. 1984
	Churchill, Canada	59°N, 94°W	Jan. 1965–Dec. 1984
	Edmonton, Canada*	54°N, 114°W	April 1958–Dec. 1984
	Goose, Canada	53°N, 60°W	Jan. 1962–Dec. 1984
	Caribou, USA	47°N, 68°W	Jan. 1963–Dec. 1984
	Bismarck, USA	47°N, 101°W	Jan. 1963–Dec. 1984
	Toronto, Canada	44°N, 79°W	Jan. 1960–Dec. 1984
	Boulder, USA	40°N, 105°W	Jan. 1964–Dec. 1984
	Nashville, USA	36°N, 87°W	March 1963–Dec. 1984
Europe	Aarhus, Denmark	56°N, 10°E	Jan. 1958–Dec. 1984
	Lerwick, United Kingdom	60°N, 1°W	Jan. 1969–Dec. 1984
	Bracknell, United Kingdom	51°N, 1°W	Jan. 1969–Dec. 1984
	Potsdam, GDR	52°N, 13°E	Jan. 1964–Dec. 1984
	Belsk, Poland	52°N, 21°E	April 1963–Dec. 1984
	Hradec Kralove, Czechoslovakia	50°N, 16°E	Aug. 1961–Dec. 1984
	Hohenpeissenberg, FRG	48°N, 11°E	Jan. 1968–Dec. 1984
	Arosa, Switzerland*	47°N, 10°E	Jan. 1958–Dec. 1984
	Mont Louis, France	42°N, 2°E	March 1962–Dec. 1979
	Vigna di Valle, Italy	42°N, 12°E	Jan. 1958–Dec. 1984
	Cagliari/Elmas, Italy	39°N, 9°E	Jan. 1958–June 1984
	Lisbon, Portugal	39°N, 9°W	Oct. 1967–Dec. 1984
India	Srinagar, India	34°N, 74°E	Feb. 1964–Nov. 1984
	Quetta, Pakistan	30°N, 67°E	Jan. 1964–Dec. 1984
	New Delhi, India	29°N, 77°E	Jan. 1960–Dec. 1984
	Varanasi, India	25°N, 83°E	Jan. 1964–Dec. 1984
	Mount Abu, India	25°N, 73°E	Nov. 1969–Feb. 1982
	Kodaikanal, India*	10°N, 77°E	Jan. 1961–Dec. 1983
Japan	Sapporo	43°N, 141°E	Feb. 1958–Dec. 1984
	Tateno*	36°N, 140°E	Jan. 1958–Dec. 1984
	Kagoshima	32°N, 131°E	Jan. 1960–Dec. 1984
Australia	Brisbane	27°S, 153°E	Jan. 1958–April 1983
	Perth	32°S, 116°E	March 1969–April 1983
	Aspendale*	38°S, 145°E	Jan. 1958–Dec. 1982
	Macquarie Island*	54°S, 159°E	April 1963–Aug. 1981
South America	Huancayo, Peru*	12°S, 75°W	March 1964–Dec. 1984
	Buenos Aires, Argentina*	35°S, 58°W	Oct. 1965–Dec. 1984
Pacific	Mauna Loa, Hawaii*	20°N, 156°W	Jan. 1964–Dec. 1984

*Nine-station network used by Hill et al. (1977).

STATISTICS

disadvantage of this model, however, is that stations within a particular region are constrained to having the same spectrum. This assumption is also made among the regional effects. Although this analysis yielded a trend estimate that differed slightly from that of Reinsel and his coworkers, most of the discrepancy can be explained by different sensitivities to extreme ozone values and to the solar variable, by different lengths of data records, and by different methods for modeling the seasonal variance (Hill et al., 1986).

Recent results reported in Chapter 4 suggest that the trend in ozone may depend on the season. For Arosa and several other northern stations, the percent losses in total ozone tended to be greater in the winter. Thus, the estimated trend may be more sensitive to the statistical treatment of the seasonal component than would otherwise have been expected. Another implication of these results is that the sensitivity of the trend estimates may be improved by concentrating on the months in which a larger trend is expected. Because monthly ozone values are autocorrelated, the estimated trends for each month will also be correlated. This feature makes it difficult to interpret the 12 individual trend estimates. However, these estimated monthly trends can be averaged to yield an estimate of the annual trend; a standard error for this estimate can be computed using the dispersion matrix of the individual estimates. Some of the statistical issues of coping with the seasonality in ozone are discussed in Section 3.

1.2 Ground-Based Ozone Profiles (Umkehr)

Statistical analysis of the Umkehr data supplied by some stations in the Dobson network is motivated by the suggestion that the main depletion of ozone due to the release of chlorofluoromethanes (CFM's) will occur at altitudes between 35 to 40 km (Umkehr layers 7 and 8). Trend analysis that concentrates on this segment of the stratosphere may be more sensitive in detecting a depletion due to CFM's than an analysis based on total column ozone. In fact, Reinsel et al. (1987) report a statistically significant negative trend in layers 7 and 8. However, these results need to be qualified in two ways. First, the average trend estimate for a particular layer cannot be interpreted as a global trend, but rather refers to the average ozone in the layer above the Dobson stations taking Umkehr data. Also, Umkehr measurements are sensitive to stratospheric aerosols (see Chapters 3 and 5 of this report). Although Reinsel's method attempts to adjust for aerosols, all the bias caused by the presence of aerosols may not be removed.

The statistical methods applied to the Dobson profile data are similar to the analysis of the total column measurements; therefore, only some specific remarks will be made. To account for the dependence of the Umkehr measurements on aerosols, an additional variable was included in the model (1). This is the atmospheric transmission of solar radiation measured at Mauna Loa, Hawaii. Although these transmission data are specific to the integrated amount of aerosols in the stratosphere over Mauna Loa, it is assumed in Reinsel et al. (1987) that a smoothed and possibly lagged version of this series may be appropriate at other locations. One weakness in this analysis is that the choices for smoothing and lagging the transmission series were not based on a specific statistical model. Nevertheless, the estimated effects due to aerosols on the different ozone layers are in agreement with theoretical predictions. Available aerosol data are discussed in Chapter 10. Reinsel and his coworkers are currently exploring the use of lidar measurements to improve aerosol corrections.

An earlier analysis of Umkehr data by Bloomfield et al. (1982) came to different conclusions from those of Reinsel et al. (1987). Specifically, the earlier analysis detected no significant negative trends. However, the earlier analysis included no attempt to correct for aerosol effects,

and was based on older data. Since the statistical methods used were similar to those of Reinsel et al. (1987) in other respects, it is to be expected that an updated analysis would give results largely in agreement with those of the later analysis.

1.3 Satellite Data

The Solar Backscatter Ultraviolet (SBUV) instrument aboard Nimbus-7 provides the most recent and the longest record of ozone measurements from a satellite (see Chapter 5). These data can be used in two different ways to improve trend detection. In contrast to the Dobson network, the Nimbus-7 ozone data provide nearly global coverage. Thus it is fairly simple to construct zonal or global series as aggregations of the raw data. Another use of the satellite data is to assess the global representativeness of the Dobson instrument network. Both of these topics are considered in Reinsel et al. (1988). This work gives an estimate of -0.35 ± 0.28 percent per year for the global trend in total ozone for November 1978 to September 1985, after adjusting for a drift in the SBUV instrument and accounting for solar activity³. Comparing the satellite measurements at the locations of the Dobson stations with the full record of measurements suggests that the average trend estimated for this network will be similar to a global trend.

This work uses the same model as that given in (1). The time scale is monthly means, and Y_t should be interpreted as some aggregation of the raw data either over blocks (10 degrees of latitude by 20 degrees of longitude), over zones (bands of 10 degrees latitude), or over the entire surface covered by the satellite (70°S latitude to 70°N latitude). In each of these cases, just as in the Dobson measurements, successive ozone values tend to be correlated. This autocorrelation must be taken into account to derive reliable uncertainty levels for estimated trends. One notable feature of this data set is its short length (7 years) relative to the Dobson data. Since this time series does not even span one solar cycle, the adjustment of the ozone series using a covariate for solar activity (such as 10.7 solar flux) is important. Reinsel et al. (1988) have included such a solar term in their analysis.

Trend analysis using the SBUV data alone is difficult because of an instrument drift (discussed in Chapter 2). Reinsel et al. (1988) estimate a linear drift to be -0.39 ± 0.11 percent per year using the Dobson network⁴. If the satellite data are adjusted by this estimated drift, then the standard error of the estimated trend must also reflect the uncertainty of the drift estimate. Reinsel et al. (1988) include the contribution of the drift uncertainty in the trend standard error, but their method is not entirely satisfactory.

The representativeness of the Dobson network was evaluated by taking a weighted average of all blocks containing the 36 stations used in Reinsel et al. (1988). When this series was subtracted from the global series, no significant trend was found in these differences ($-.06 \pm .12$ percent per year). Although these results suggest that a trend in the Dobson network may be similar to a global trend, there are some problems with this comparison. The blocks are not point measurements of total column ozone but are themselves averages over a substantial amount of surface area. This may cause closer agreement with the global series than might otherwise occur if one used the measurements taken at specific locations. Also, in the actual Dobson analysis,

³ This trend estimate has been updated to -0.28 ± 0.22 percent per year for the period November 1978 through December 1986 (Reinsel, 1988, personal communication).

⁴ This drift estimate has been updated to $-.40 \pm 0.11$ percent per year for the period November 1978 through December 1986 (Reinsel, 1988, personal communication).

STATISTICS

individual trends are estimated for each station and then combined. This differs from first forming an average series from the blocks and then estimating the average trend from this single series.

2.0 TEMPORAL AND SPATIAL CORRELATION

An important contribution of statistical methods to problems such as estimation of trends in ozone data is attaching an appropriate measure of uncertainty to any trend estimate. In this section we shall review the calculation of such measures and discuss their validity.

2.1 Least-Squares Estimates

The calculation of the least-squares slope of a set of data is the most familiar example of trend estimation. Suppose that the data are y_1, y_2, \dots, y_n . Then the least-squares estimate of slope is

$$\hat{\omega} = \frac{\sum_{t=1}^n (t - \bar{t})(y_t - \bar{y})}{\sum_{t=1}^n (t - \bar{t})^2} \quad (2)$$

where

$$\bar{t} = (n + 1)/2 \text{ and } \bar{y} = (1/n) \sum_{t=1}^n y_t.$$

The full equation of the fitted line is

$$y = \bar{y} + \hat{\omega}(t - \bar{t}).$$

The *residuals* are the vertical distances from the data points (t, y_t) to the line, and are given by

$$r_t = y_t - \hat{y}_t = y_t - \{\bar{y} + \hat{\omega}(t - \bar{t})\}.$$

The *residual sum of squares* is just

$$\sum_{t=1}^n r_t^2,$$

and the *residual mean square* is this divided by the *degrees of freedom* $(n - 2)$,

$$s^2 = \frac{1}{n-2} \sum_{t=1}^n r_t^2.$$

The *standard error* of the slope estimate $\hat{\omega}$ (as it is usually calculated) is

$$SE(\hat{\omega}) = \frac{s}{\sqrt{\sum_{t=1}^n (t - \bar{t})^2}}, \quad (3)$$

and it is common for the estimated slope to be reported as " $\hat{\omega} \pm SE(\hat{\omega})$ " or, for reasons described in the next section, as " $\hat{\omega} \pm 2 SE(\hat{\omega})$ ". But what meaning can be attached to such a report?

2.2 Interpretation of Standard Error

We can give a firm interpretation to a standard error such as $SE(\hat{\omega})$ only by reference to some *model* for the randomness in the data. The simplest such model is

$$y_t = \mu + \omega(t - \bar{t}) + \epsilon_t, \quad (4)$$

where $\{\epsilon_1, \epsilon_2, \dots, \epsilon_n\}$ are random errors, independently drawn from a Gaussian distribution with mean value 0 and variance σ^2 . The constants μ , ω , and σ are the (statistical) *parameters* of the model, and \bar{y} , $\hat{\omega}$, and s are *estimates* of these parameters. The implication of such a model is that the observed set of data $\{y_1, y_2, \dots, y_n\}$ is only one out of an infinitely large set of possible data sequences, each with different values of the ϵ 's. The observed data are a *sample* (of size 1) from the *population* of possible sequences.

Since each possible sequence gives rise to a different value of $\hat{\omega}$, the model implies a distribution for $\hat{\omega}$, called its *sampling distribution*. The variance of this distribution is

$$\text{var}(\hat{\omega}) = \frac{\sigma^2}{\sum_{t=1}^n (t - \bar{t})^2}, \quad (5)$$

and, consequently, the standard error calculated in (3) can be regarded as an estimate of the square root of this variance.

It follows that for an appropriate constant $t_{n-2}^{.95}$, the range of values

$$\hat{\omega} \pm t_{n-2}^{.95} SE(\hat{\omega})$$

has a 95 percent chance of containing the "true" slope value, ω , or, in a certain sense,

$$Pr\{\hat{\omega} - t_{n-2}^{.95} SE(\hat{\omega}) \leq \omega \leq \hat{\omega} + t_{n-2}^{.95} SE(\hat{\omega})\} = .95 \quad (6)$$

Since the tabulated values for $t_{n-2}^{.95}$ are all at least 1.96, and for $n > 60$ are at most 2, the interval is often approximated by

$$\hat{\omega} \pm 2SE(\hat{\omega}).$$

Thus, "2 σ " limits can be interpreted as giving an approximate 95 percent confidence interval.

2.3 Limitations of the Model

Evidently the credibility of the standard error (3) depends on the credibility of the model (4), in light of the data. It is often clear by cursory inspection that the Gaussian distribution is not a good model for the distribution of the errors ϵ_t . The Gaussian distribution is symmetric about its center and has relatively short tails, behavioral aspects that are often not shared by real data. However, it is known that the confidence interval statement (6) is not drastically affected by such deviations from the model (the effects of such deviations in the simpler case of estimating a mean are discussed by Benjamini, 1983).

A more serious problem is that the model (4) states that the data are *independent* of each other, and hence *uncorrelated*. In many sets of real data, however, especially those collected sequentially

STATISTICS

in time (*time series data*), cursory inspection reveals *serial (or temporal) correlation* in the data. Unfortunately, the effect of correlations among the data, including serial correlation, is generally to invalidate any confidence interpretation of the conventional standard error formula (3).

How is correlation visible? Positive correlation among consecutive observations means that a value higher than expected (that is, one with a positive error ϵ) is likely to be followed by another observation with a positive ϵ . Such *persistence* of deviations above or below what is expected is characteristic of many real series, including ozone data and most of the related meteorological data. Figure 1 shows annual mean ozone levels at Arosa, Switzerland, 1933 to 1982, from Birrer (1975) and Dütsch (1984b). Also shown is the (least-squares) regression line for the data, with equation

$$y = 336.4 - 0.1648 (\text{year} - 1957.5).$$

The occurrence of several values in a row above or below the regression line is evidence of positive serial correlation, though it is less strong in this series than in many. Figure 2 shows the same data with least-squares lines fitted through data for several successive 10-year periods. This is essentially the same as the analysis of Bishop and Hill (1982). The coefficients of the lines are given in Table 2. The average of the nine SE's is 0.819, whereas the standard deviation of the calculated trends is 1.199. Thus the calculated trends show 46 percent more variation than their standard errors suggest they should. For series with stronger correlation between consecutive values, such as monthly station data and regional or global average series, the actual variability can exceed the estimated standard error by much more than in this case.

Where does this leave us? The standard formula (3) is, in general, meaningful only in the context of the model (4), but this model is untenable for most of the data we need to analyze for trend. Evidently we need a more tenable model, and a new formula for standard error that has the desired confidence interpretation (6) in the context of that model.

We shall see that other models may suggest other formulas for slope estimates, as well as for their standard errors. In general, these other slope estimates differ little from the ordinary least-squares estimates (2), and, in fact, (2) is asymptotically efficient in the presence of stationary autocorrelated noise (Grenander, 1954). Thus, the problem lies mainly in obtaining valid standard errors, not in calculating the slope estimate itself.

Table 2. Coefficients of least-squares lines

Start year	End year	Centercept ^a	Slope	SE (slope)
1933	1942	340.633	1.526	1.276
1938	1947	338.458	-0.678	1.397
1943	1952	335.892	1.753	0.676
1948	1957	337.450	0.224	0.799
1953	1962	339.600	0.490	0.747
1958	1967	337.976	-1.915	0.754
1963	1972	335.576	0.643	0.727
1968	1977	334.392	-1.166	0.578
1973	1982	330.375	0.044	0.440

^a The *centercept* of the line is its height at the midpoint of the interval to which it is fit.

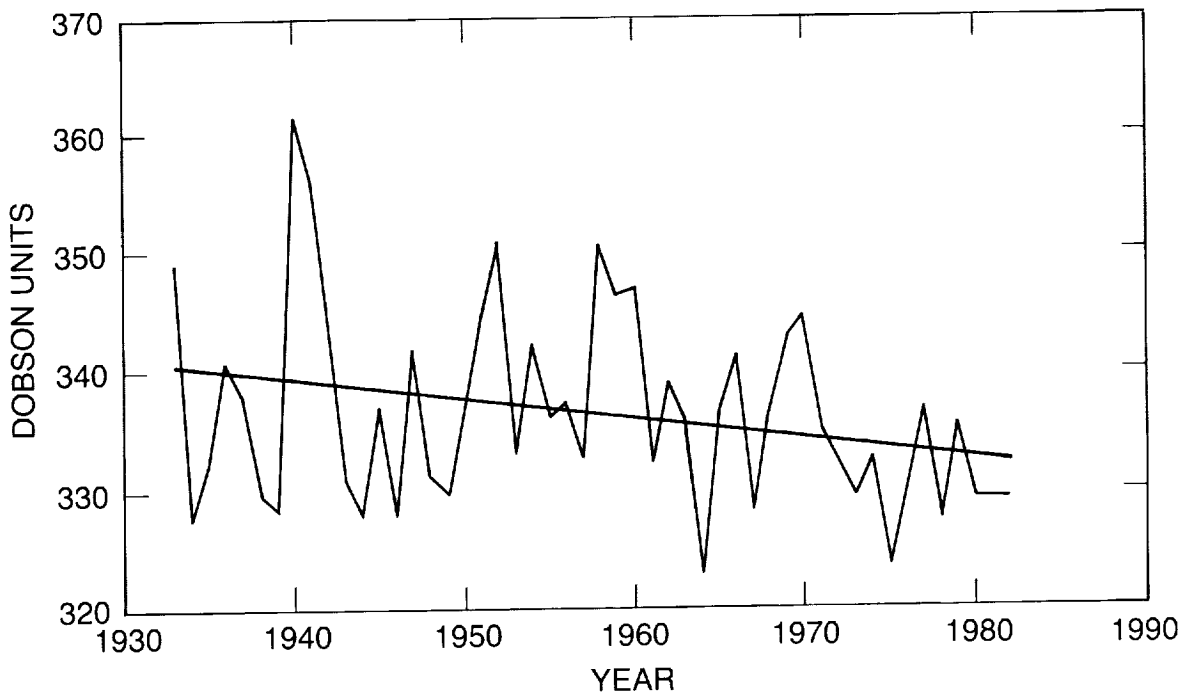


Figure 1: Annual mean ozone levels at Arosa, Switzerland, 1983–1982. (Unweighted averages of monthly means, with missing months replaced by least-squares estimates.)

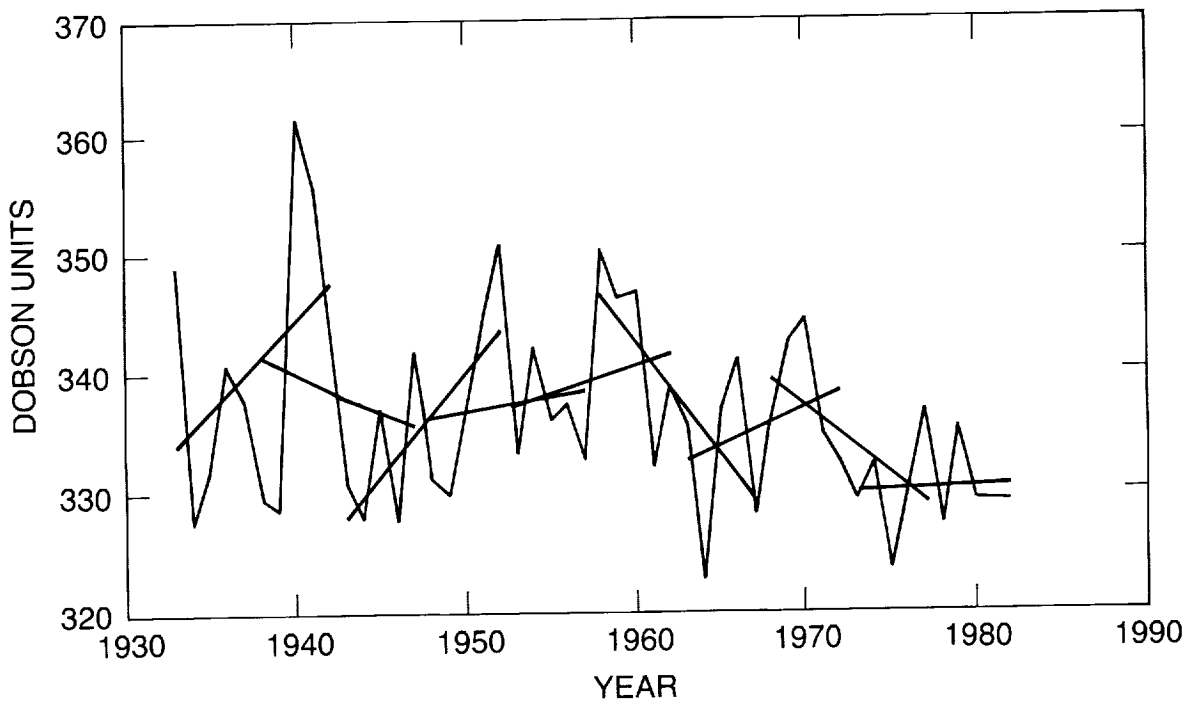


Figure 2: Arosa data with least-squares fitted lines.

2.4 An Elementary Model for Temporal Correlation

Models for serially correlated data have been discussed extensively in the statistical literature (see, for example, Box and Jenkins, 1976). One of the simplest is the (first-order) *autoregressive model*

$$\eta_t = \phi\eta_{t-1} + \epsilon_t, \quad |\phi| < 1, \quad (7)$$

where the ϵ_t 's are, as in (4), independent from mean 0 and variance σ^2 . If we introduce the *backshift operator* B , defined by

$$B\eta_t = \eta_{t-1},$$

and more generally

$$B^h\eta_t = \eta_{t-h}, \quad -\infty < h < \infty,$$

the model (7) may be written

$$\eta_t = \phi B\eta_t + \epsilon_t$$

whence

$$(1 - \phi B)\eta_t = \epsilon_t$$

and

$$\eta_t = (1 - \phi B)^{-1}\epsilon_t.$$

For this model, the serial covariances (or *autocovariances*) are

$$\gamma_h = \text{cov}(\eta_t, \eta_{t-h}) = \frac{\sigma^2\phi^{|h|}}{1 - \phi^2}, \quad -\infty < h < \infty$$

and the serial correlations are

$$\rho_h = \text{corr}(\eta_t, \eta_{t-h}) = \phi^{|h|}, \quad -\infty < h < \infty. \quad (8)$$

Since ϕ can be arbitrarily close to 1, this model can display correlations that are also close to 1, and that die away very slowly as the time separation h increases.

Now suppose that we wish to estimate a trend in the presence of correlated errors with the structure (7). That is, suppose that we wish to estimate ω in the equation

$$y_t = \mu + \omega(t - \bar{t}) + \eta_t,$$

where $\{\eta_t\}$ satisfies (7). If we know the value of ϕ , the simplest solution is to construct a new set of data

$$\begin{aligned}
 y_t^* &= y_t - \phi y_{t-1} \\
 &= \{\mu + \omega(t - \bar{t}) + \eta_t\} - \phi\{\mu + \omega(t - 1 - \bar{t}) + \eta_{t-1}\} \\
 &= (1 - \phi)(\mu + \omega/2) + \omega(1 - \phi)(t - \bar{t} - 1/2) + \eta_t - \phi\eta_{t-1} \\
 &= (1 - \phi)(\mu + \omega/2) + \omega(1 - \phi)(t - \bar{t} - 1/2) + \epsilon_t,
 \end{aligned}$$

for $t = 2, \dots, n$. If we write

$$x_t^* = (1 - \phi)(t - \bar{t} - 1/2)$$

and

$$\mu^* = (1 - \phi)\mu + (1 - \phi)\omega/2,$$

then the modified data satisfy

$$y_t^* = \mu^* + \omega x_t^* + \epsilon_t,$$

which is in the same form as the original equation (4), with errors ϵ_t that are now *uncorrelated*. It is therefore legitimate to estimate ω by least-squares, and to report its standard error as in equation (3). The resulting estimate is

$$\hat{\omega}_{ar1} = \frac{\sum_{t=2}^n x_t^*(y_t^* - \bar{y}^*)}{\sum_{t=2}^n x_t^{*2}}$$

with standard error

$$SE(\hat{\omega}_{ar1}) = \frac{s_{ar1}}{\sqrt{\sum_{t=2}^n x_t^{*2}}}$$

where

$$s_{ar1}^2 = \frac{1}{n-3} \sum_{t=2}^n (y_t^* - \bar{y}^* - \hat{\omega}_{ar1} x_t^*)^2.$$

It may be shown that if n is large and $|\phi|$ is not close to 1, the new slope estimate $\hat{\omega}_{ar1}$ is very close to the estimate $\hat{\omega}$ of equation (2). However, the new standard error may be quite different from the earlier version, and is typically larger. In fact, we can show that if n is large and $|\phi|$ is not close to 1, then the (valid) standard error of $\hat{\omega}_{ar1}$ is larger than the (invalid) standard error of the least-squares estimate $\hat{\omega}$ by the factor

$$\sqrt{(1 + \phi)/(1 - \phi)}.$$

For the Arosa annual average data, the estimated value of ϕ is around 0.25, which would make this factor approximately 1.29. Since we observed 46 percent more variation among the

STATISTICS

slopes than was suggested by the least-squares standard error, rather than 29 percent, there is even more variability among the calculated trends than is predicted by the model (7).

Reinsel et al. (1987) found the month-to-month correlation for SBUV total ozone column data averaged from 70°S to 70°N to be around 0.84, which would make this factor 3.39. Thus, for ozone data averaged over a large region, in this case most of the globe, the effect of ignoring serial correlation can be a reported standard error of less than a third of its true value. Reinsel et al. (1988) give several illustrations of the difference between the valid and invalid standard errors.

In practice, of course, we will not know the value of ϕ , but it may be estimated from residuals and, provided the series length is adequate, used essentially as if it were known. An iterative procedure in which ϕ and ω are updated alternately was suggested by Cochrane and Orcutt (1949), and has been shown to yield maximum conditional likelihood estimates (Sargan, 1964). The procedure is discussed by Shumway (1988, Section 3.5).

2.5 More General Temporal Models

Equation (7) is often not the appropriate model for a given set of data; in practice, serial correlations may not show the simple exponential decay of equation (8). However, it is the simplest of a family of models (the ARMA family) that can be used in this way to model serial correlation and to provide valid standard errors for parameter estimates. The ARMA model of order (p, q) has the form

$$\eta_t = \sum_{r=1}^p \phi_r \eta_{t-r} + \sum_{s=0}^q \theta_s \epsilon_{t-s}. \quad (9)$$

In terms of the backshift operator, this may be written

$$\eta_t = \frac{\theta(B)}{\phi(B)} \epsilon_t$$

where the polynomials $\phi(z)$ and $\theta(z)$ are defined by

$$\phi(z) = 1 - \sum_{r=1}^p \phi_r z^r, \quad \theta(z) = \sum_{s=0}^q \theta_s z^s.$$

The constraint $|\phi| < 1$ in the first-order model is generalized to the requirements

$$\phi(z) \neq 0 \text{ for } |z| \leq 1, \quad \theta(z) \neq 0 \text{ for } |z| < 1.$$

For this model, the autocorrelations

$$\rho_h = \text{corr}(\eta_t, \eta_{t-h})$$

cannot be written down explicitly, but satisfy the difference equation

$$\rho_h = \sum_{r=1}^p \phi_r \rho_{h-r}, \quad h > q.$$

They therefore still decay to zero at an exponential rate as $h \rightarrow \infty$, but not as a simple exponential sequence.

As in the case of the AR(1) model (7), the slope of a trend line should be estimated not by ordinary least-squares, but by some method that takes the covariance structure of the data into account. Various methods are available, and some are implemented in the more complete statistical packages. It is again true that the slope estimate itself is generally close to the one obtained by ordinary least-squares, but its standard error may be very different when calculated appropriately. The approximate ratio of the correct standard error to the incorrect one can again be calculated, but it is more easily expressed in terms of the *power spectrum* of the model than its autocovariances.

The power spectrum of a stationary time series is the function whose Fourier coefficients are the autocovariances

$$s(f) = \sum_{h=-\infty}^{\infty} \gamma_h \epsilon^{-2\pi i f h}, 0 \leq f < 1,$$

from which it follows that

$$\gamma_h = \int_0^1 e^{2\pi i f h} s(f) df, -\infty < h < \infty.$$

The power spectrum of the ARMA(*p*, *q*) model (9) is

$$s_{ARMA}(f) = \sigma^2 \frac{|\theta(e^{2\pi i f})|^2}{|\phi(e^{2\pi i f})|^2}.$$

Grenander (1954) showed that the variance of the sampling distribution of a trend estimated from a stretch of data of length *n* is, for large *n*, approximately

$$\text{var}(\hat{\omega}) = \frac{s(0)}{\sum_{t=1}^n (t - \bar{t})^2}, \tag{10}$$

Comparison with equation (5) shows that the factor σ^2 in the numerator has been replaced by $s(0)$, the power spectrum evaluated at zero frequency. Equation (10) can be used as the basis for computing the approximate standard error of the trend estimate, or merely to get an indication of how much the standard error differs from the result given by the formula (3), the ratio being just

$$\sqrt{s(0) / \int_0^1 s(f) df}.$$

2.6 Spatial Correlation

In the previous sections we discussed the complications that arise when we analyze data collected over time, with correlation among observations that are close together in time (serial correlation, or *temporal* correlation). Measurements made close together in *space* also tend to be correlated, and when such measurements are analyzed jointly, their *spatial* correlation also needs to be taken into account.

One general approach to analysis of spatiotemporal data is based on models generalized from the strictly temporal models described above. However, this approach requires the data to be

STATISTICS

collected on a regular grid of locations, and to show some homogeneity in their correlation structure. One or both of these features is absent in most of the data that have been collected in studies of ozone and other atmospheric trends. However, more ad hoc solutions can be found for certain problems.

One such problem is the need to combine quantities calculated from data collected at different locations. Suppose that $\hat{\theta}_1$ and $\hat{\theta}_2$ are estimates of similar quantities at two locations. Each $\hat{\theta}$ might be a trend estimate, or an average ozone level over a decade, or a change in such an average from one decade to the next. The standard error of the average

$$\hat{\theta} = (\hat{\theta}_1 + \hat{\theta}_2)/2$$

is given by

$$SE(\hat{\theta}) = \sqrt{\text{var}(\hat{\theta})}$$

where

$$\text{var}(\hat{\theta}) = (1/4) \{ \text{var}(\hat{\theta}_1) + \text{var}(\hat{\theta}_2) + 2\text{cov}(\hat{\theta}_1, \hat{\theta}_2) \}.$$

The two variance terms can usually be obtained from the analysis of the data for locations 1 and 2 separately, but the covariance term depends on the joint behavior of the two sets of data, and therefore can be calculated only from a joint analysis. While this is not a difficult analysis to carry out, it is not one that the commonly available statistical packages are set up to handle. Reinsel and Tiao (1987) describe a method that amounts to doing just this, in their analysis of an entire Dobson network, but the method is not easy to implement with standard software. As a result, it is more convenient to calculate summary statistics for a number of locations in a slightly different way.

Consider, for instance, the problem of calculating an average trend for all Dobson stations in a certain latitude band. Since it is straightforward to calculate a trend for each station, it might seem that the way to proceed is to simply combine the individual trends. However, to compute the standard error for this average we would need to know all the covariances among the individual station trends. We can, instead, form an average ozone time series for the band, then estimate the trend in this single series. The standard error of the resulting estimate may then be obtained in the usual way. The estimated trend in the average series is, in general, close to the average of the individual trends, and may actually be a more appropriate quantity to consider.

The weakness of this approach is that the analysis of the average series can account only for the statistical fluctuations that are visible in the average. Thus, phenomena that induce spurious trends in the individual station records, for example instrument drift, pass undetected, while in Reinsel and Tiao's approach they show up as variations among the individual trend estimates. As a result, the standard error obtained from analysis of an average series may need to be inflated to allow for such phenomena, while the standard error calculated from Reinsel and Tiao's method automatically allows for them. Neither approach can handle spurious trends common to all stations, so in either case some allowance must be made for these.

3.0 SEASONALITY IN OZONE DATA

In this section we review various ways in which ozone data show seasonal behavior, the problems such behavior raises, and some of the solutions used.

3.1 Seasonal Structure in the Mean

Seasonal structure is one aspect of many time series that needs to be considered when estimating a trend. It is usually easy to separate seasonal behavior from trend, so the issue is not one of confusion between the two so much as estimating the size of the random errors in the data.

There are two basic strategies for coping with seasonality in the mean. One is to use *seasonal adjustment* to remove the seasonal behavior, and then to estimate trend from the *seasonally adjusted* data. The second is to fit a model that includes both seasonal structure and a trend term, so that both parts are estimated simultaneously. The former is preferred in exploratory analysis as it allows more flexibility in estimating the trend. For instance, a graph of the adjusted data will often suggest what kind of trend is actually present, and will typically provide a preliminary estimate of its magnitude. By contrast, simultaneous estimation is preferable when a model has been chosen and its parameters are being estimated. One advantage of simultaneous estimation is that it usually provides standard errors for all estimated parameters, as well as their correlations.

In either case, it is necessary to specify the seasonal structure to be removed or incorporated into the model, respectively. The simplest approach is to allow an arbitrary mean for each month⁵. If we write the data as

$$y_t = S_t + z_t,$$

where S_t and z_t represent the seasonal and nonseasonal parts of the data, respectively, then this amounts to putting

$$S_t = \mu_i \text{ if data month } t \text{ falls in calendar month } i, i = 1, 2, \dots, 12.$$

Here, μ_1 is the mean of January data, μ_2 is the mean of February data, and so on.

This approach has the merits of simplicity and ease of interpretation, but in short series it may be undesirable to use as many as 12 parameters to describe seasonal structure. An alternative approach is to use a sine-cosine expansion. In this case, we put

$$S_t = \mu + \sum_{j=1}^J \{A_j \cos(2\pi jt/12) + B_j \sin(2\pi jt/12)\}$$

where $J \leq 5$, using $2J + 1$ parameters. Often $J = 1$ or $J = 2$ is sufficient, corresponding to fitting an annual wave with three parameters, or annual and semiannual waves requiring five parameters, respectively. If we set $J = 6$ with the constraint $B_6 = 0$, there are again 12 parameters; this is effectively the same as allowing an arbitrary set of monthly means.

Figure 3 shows the results of these two approaches for the monthly Arosa data. The asterisks indicate the monthly means; the curve is constructed from a sine-cosine expansion with $J = 2$ (estimated by ordinary least-squares). This two-frequency model fits most of the monthly means

⁵ For ease of exposition we deal only with the case of monthly data. The modifications necessary for other types of seasonal behavior are clear.

STATISTICS

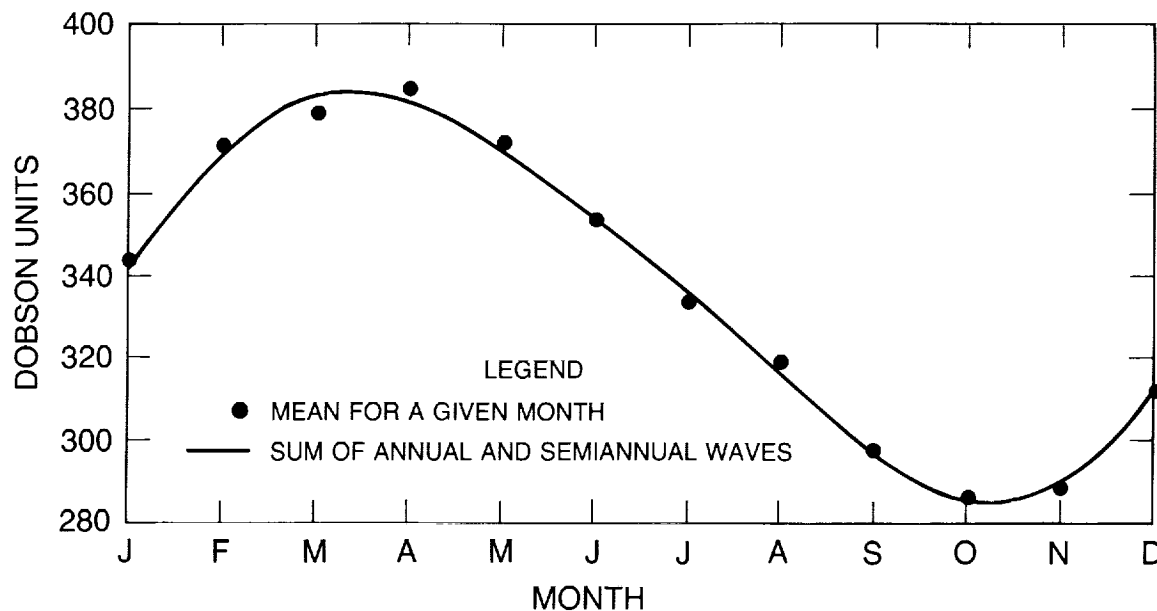


Figure 3: Seasonal structure of monthly Arosa data.

well in the graph, but the lack of fit in March and April could be critical in a trend study (see Section 3.2 below).

3.2 Seasonal Structure In the Trend

The issue of seasonal structure in the mean of a series discussed in the previous section may also extend to estimating a trend, if theory or observation suggests that the trend may vary from season to season.

Suppose, for instance, that trend is being measured by a ramp function such as

$$r_t = \begin{cases} \lambda & \text{if } t < t_0 \\ \lambda + \omega(t - t_0) & \text{if } t \geq t_0 \end{cases}$$

$$= \lambda + \omega(t - t_0)_+,$$

where $(t - t_0)_+$ is defined by

$$(t - t_0)_+ = \begin{cases} 0 & \text{if } t < t_0 \\ (t - t_0) & \text{if } t \geq t_0. \end{cases}$$

The function r_t has the constant level λ up to month t_0 , and increases with slope ω units per month after month t_0 . As in the previous section, we have various ways of allowing the magnitude of the trend to vary from month to month. The simplest is to replace the single λ by 12 λ 's and the single ω by 12 ω 's:

$$r_t = \lambda_i + \omega_i(t - t_0)_+ \text{ if data month } t \text{ falls in calendar month } i.$$

Seasonal trend estimates of this form are reported in Chapter 4.

Again, however, we might not want to allow completely arbitrary variation in the trends from one month to the next. One alternative would be to use sine-cosine expansions as before:

$$r_t = \lambda_0 + \sum_{j=1}^J \{A_j \cos(2\pi jt/12) + B_j \sin(2\pi jt/12)\} + \left[\omega_0 + \sum_{j=1}^J \{C_j \cos(2\pi jt/12) + D_j \sin(2\pi jt/12)\} \right] (t - t_0)_+.$$

Notice that we have used the same number of terms in each expansion. Statistical considerations such as lack of significance of some coefficients might suggest dropping terms from one sum but not the other, but care would have to be used. Omission of significant terms from one sum would introduce bias into estimates of coefficients in the other, and possibly into other coefficients in the same sum. In particular, bias could arise if a sine-cosine expansion were used for, say, the level term, and arbitrary constants were used for the trend, since using arbitrary constants is effectively the same as taking $J = 6$ (and omitting the final sine term).

3.3 Seasonal Structure in the Correlations

In Section 2 we have discussed the use of time-series models to represent the correlation among measurements such as ozone columns at different times at the same location (or geographical region). One way in which those models are not sufficiently general is that they have *stationary* covariance structure:

$$\text{cov}(y_t, y_{t-h}) = \text{a function only of } h.$$

However, most ozone time series have covariances that depend on the season as well as the time separation h . This is most easily seen in the monthly dependence of the standard deviation. As was mentioned in Section 1.1, failure to allow for such seasonality in covariance structure distorts any analysis by placing equal weight on the more variable winter data and the less variable summer data.

Two approaches have emerged for coping with this problem. Reinsel and his coworkers have developed and exploited a method that can be described as seasonally weighted least-squares, while the values reported in Chapter 4 were obtained essentially by standardization of the data before fitting the trend model. The two approaches may be compared in terms of a corresponding model for the noise term η_t . In each case, the analysis may be interpreted as using a modified ARMA model (cf. equation 9). Reinsel's approach corresponds to the model

$$\eta_t = \frac{\theta(B)}{\phi(B)} (\sigma_t \epsilon_t),$$

while the approach used in this report corresponds to

$$\eta_t = \sigma_t \frac{\theta(B)}{\phi(B)} \epsilon_t.$$

In each case, the scale factors σ_t are periodic, and reflect the seasonal dependence of the standard deviation of the noise η_t and of the innovations ϵ_t , respectively. Both general models appear plausible, but studies of which fits ozone data better have not been performed in depth.

4.0 Summary

Ready, widespread acceptance of the results of a scientific investigation depends critically on the credibility of the study, and, in the case of a data-oriented study, this in turn depends largely on two factors: the quality of the data on which the study is based and the quality of the subsequent analysis of those data. Data quality for each of the measuring systems is discussed in the relevant chapters; here we offer only broad comments. The primary focus of this appendix is on data analysis techniques, about which we offer more specific suggestions.

- *Trend estimates*—There are many ways to qualify the trend in a set of data, including fitting a straight line, fitting a ramp (or hockey stick) function, or comparing averages over different time windows. In each case, the resulting quantity should be accompanied by an appropriate standard error.
- *Standard errors*—A standard error has meaning only in the context of being a model for the way in which the data were sampled. If the data show evidence of spatial or temporal correlation, the sampling model must reflect this. Computer software for building the required sampling models and calculating the corresponding trend estimates and standard errors is widely available and should be used more extensively.
- *Current results*—Trend estimates based on fitting ramp functions reported in Chapter 4, and those of Reinsel, Tiao, and their coworkers, adequately account for serial correlation and its seasonal structure, and represent state-of-the-art estimates. Estimates of trends from Total Ozone Mapping Spectrometer (TOMS) data, also reported in Chapter 4, allow for serial correlation, but not for its seasonal structure. Although not state of the art, the results should be close. Standard errors of other trend estimates obtained by least-squares fitting without allowance for serial correlation may be incorrect by factors of more than three.
- *Ground-based total ozone column data*—It has been demonstrated that the quality of Dobson total ozone column data can be improved substantially by retroactive application of corrections based on calibration changes. This is best carried out by complete recalculation of each day's data on the basis of corrected algorithms, but useful improvements can be made by correcting monthly averages. Stations should be urged to give a higher priority to such adjustments to historical data, and to ensuring publication of the adjusted data by the World Ozone Center.
- *Ground-based ozone profile data*—The largest remaining question about the quality of the ozone profile data obtained by the Umkehr technique is the impact of aerosols. This question will have to be resolved before the Umkehr network can fulfill its dual roles of providing ground-based information about trends in ozone profiles and of providing ground truth for the validation of satelliteborne instruments.
- *Satellite ozone measurements*—The realization that the effect of diffuser plate degradation on Nimbus-7 cannot be uniquely separated from other instrument changes underscores the difficulty of maintaining measurement stability with satellite-based systems. This illustrates the continuing need for cross-checking all types of measurements, a need about which there has been a tendency to become complacent.

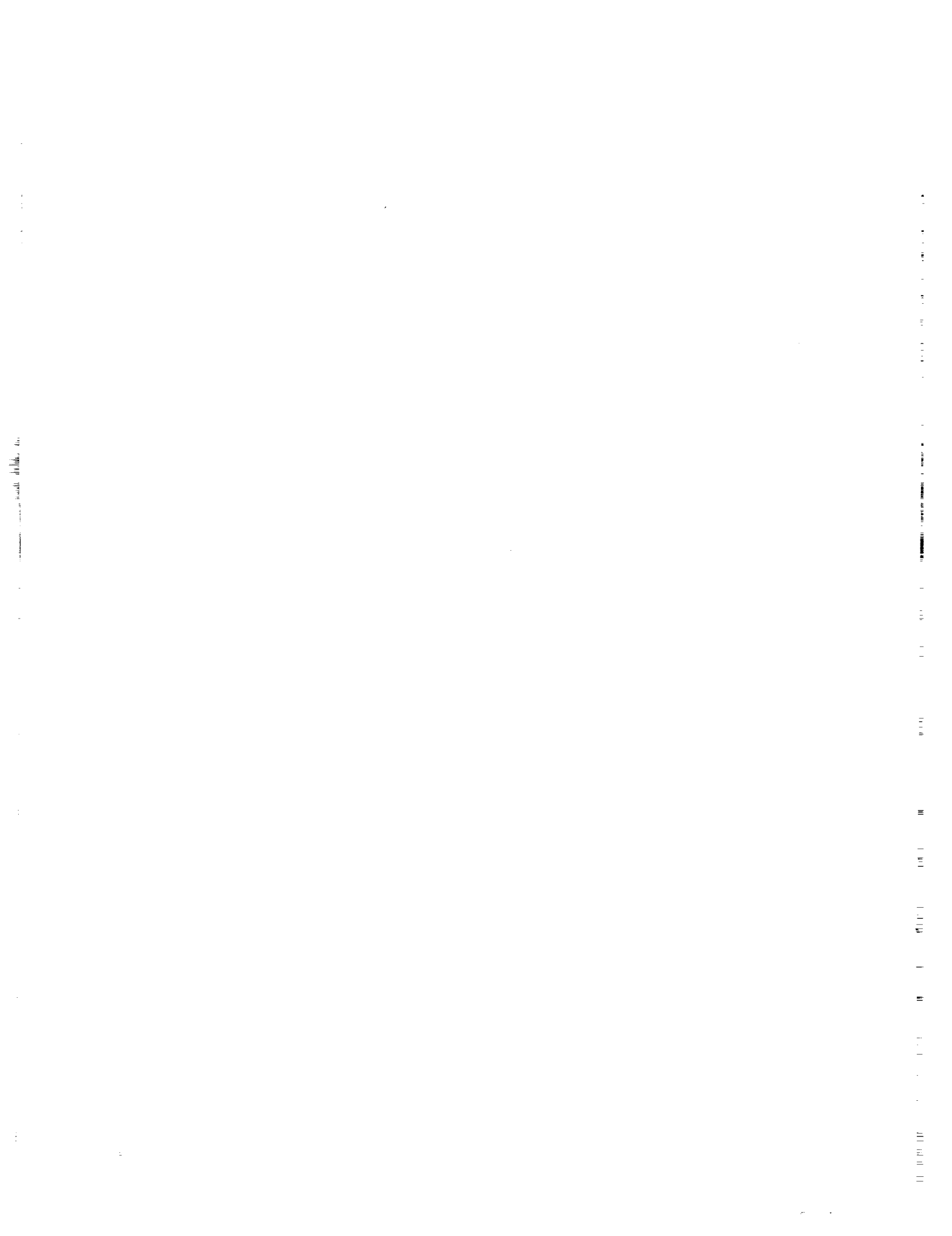
omit
to
LND

APPENDIX B

List of Contributors

1.4.14 11

PRECEDING PAGE BLANK NOT FILMED



Appendix B

List of Contributors

Ozone Trends Panel

D. Albritton	NOAA Aeronomy Laboratory, Boulder, CO
P. Bloomfield	North Carolina State University, Raleigh
R. Bojkov	Atmospheric Environment Service, Downsview, Ontario, Canada
D. Ehhalt	Institute for Chemistry, Julich, Federal Republic of Germany
P. Fraser	CSIRO, Aspendale, Australia
J. Gille	NCAR, Boulder, CO
D. Hartmann	University of Washington, Seattle, WA
R. Hudson	NASA/Goddard Space Flight Center, Greenbelt, MD
I.S.A. Isaksen	University of Oslo, Oslo, Norway
H. Johnston	University of California, Berkeley
J. Mahlman	NOAA Geophysical Fluid Dynamics Laboratory, Princeton, NJ
J.J. Margitan	Jet Propulsion Laboratory/NASA Headquarters, Washington, DC
M.P. McCormick	NASA/Langley Research Center, Hampton, VA
M. McFarland	E.I. DuPont de Nemours & Company, Wilmington, DE
F. Ormond, Executive Secretary	ARC/NASA, Washington, DC
C. Rodgers	Oxford University, Oxford, England
F.S. Rowland	University of California, Irvine
M. Schoeberl	NASA/Goddard Space Flight Center, Greenbelt, MD
R. Stolarski, Vice Chair	NASA/Goddard Space Flight Center, Greenbelt, MD
R. Turco	R&D Associates, Marina del Rey, CA
R.T. Watson, Chair	NASA Headquarters, Washington, DC

Reviewers

J. Barnett	Oxford University, Oxford, England
R.J. Cicerone	NCAR, Boulder, CO
S. Fels	NOAA, Geophysical Fluid Dynamics Laboratory, Princeton, NJ
N. Krull	Federal Aviation Administration, Washington, DC
M.J. Kurylo	NBS/NASA Headquarters, Washington, DC
M. McIntyre	University of Cambridge, Cambridge, England
G. Megie	Service d'Aeronomie, CNRS, Verrieres, le Buisson, France
M. Prather	Goddard Institute for Space Studies, New York, NY
H. Rodhe	University of Stockholm, Sweden
A. Schmeltekopf	NOAA, Environmental Research Laboratory, Boulder, CO
N. Sundararaman	World Meteorological Organization, Geneva, Switzerland
G. Visconti	University of Aquila, Aquila, Italy
S. Wofsy	Harvard University, Cambridge, MA

CONTRIBUTORS

Working Groups

Executive Summary

Robert T. Watson, NASA Headquarters, Washington, DC, Chair

Ozone Trend Panel Members
Ozone Trend Panel Reviewers

Chapter 1 Introduction

Robert T. Watson, Chair, Ozone Trends Panel

Chapter 2 Spacecraft Instrument Calibration and Stability

J. Gille, Chair, National Center for Atmospheric Research, Boulder, Colorado

P. Feldman	Johns Hopkins University, Baltimore, Maryland
R. Hudson	NASA/Goddard Space Flight Center, Greenbelt, Maryland
J. Lean	Naval Research Laboratory, Washington, D.C.
R. Madden	National Bureau of Standards, Gaithersburg, Maryland
L. McMaster	NASA/Langley Research Center, Hampton, Virginia
G. Mount	NOAA, Boulder, Colorado
G. Rottman	LASP, University of Colorado, Boulder
P.C. Simon	Institute d'Aeronomie Spatiale de Belgique, Brussels, Belgium

Chapter 3 Information Content of Ozone Retrieval Algorithms

C. Rodgers, Chair, Oxford University, Oxford, England

P.K. Bhartia	Science Applications Research, Lanham, Maryland
W.P. Chu	NASA/Langley Research Center, Hampton, Virginia
R. Curran	NASA Headquarters, Washington, D.C.
J. DeLuisi	NOAA, Boulder, Colorado
J. Gille	NCAR, Boulder, Colorado
R. Hudson	NASA/Goddard Space Flight Center, Greenbelt, Maryland
C. Mateer	Atmospheric Environment Service, Downsview, Ontario, Canada
D. Rusch	University of Colorado, Boulder
R.J. Thomas	University of Colorado, Boulder
R. Turco	R&D Associates, Marina del Rey, California
W. Wiscombe	NASA/Goddard Space Flight Center, Greenbelt, Maryland

Chapter 4 Trends in Total Column Ozone Measurements

F.S. Rowland, Chair, University of California, Irvine

J. Angell	NOAA, Rockville, Maryland
W. Attmannspacher	Deutscher Wetterdienst, Hohenpeissenberg, Federal Republic of Germany

P. Bloomfield	North Carolina State University, Raleigh
R. Bojkov	Atmospheric Environment Service, Downsview, Ontario, Canada
N. Harris	University of California, Irvine
W. Komhyr	NOAA, Boulder, Colorado
M. McFarland	E.I. DuPont de Nemours & Company, Wilmington, Delaware
R. McPeters	NASA/Goddard Space Flight Center, Greenbelt, Maryland
R. Stolarski	NASA/Goddard Space Flight Center, Greenbelt, Maryland

Chapter 5 Trends in Ozone Profile Measurements

H. Johnston, Chair, University of California, Berkeley

A. Aikin	NASA/Goddard Space Flight Center, Greenbelt, Maryland
R. Barnes	Chemal, Inc., Wallops Island, Virginia
S. Chandra	NASA/Goddard Space Flight Center, Greenbelt, Maryland
D. Cunnold	Georgia Institute of Technology, Atlanta, Georgia
J. DeLuisi	NOAA, Boulder, Colorado
J. Gille	NCAR, Boulder, Colorado
R. Hudson	NASA/Goddard Space Flight Center, Greenbelt, Maryland
M.P. McCormick	NASA/Langley Research Center, Hampton, Virginia
L. McMaster	NASA/Langley Research Center, Hampton, Virginia
A.J. Miller	NOAA/NWS/Climate Analysis Center, Washington, D.C.
R. Nagatani	NOAA/NWS/Climate Analysis Center, Washington, D.C.
W. Planet	NOAA NESDIS, Washington, D.C.
E. Remsberg	NASA/Langley Research Center, Hampton, Virginia
D. Rusch	University of Colorado, Boulder
C. Trepte	ST Systems Corporation, Hampton, Virginia
R. Veiga	NRC/NSF, Hampton, Virginia
P. Wang	STC, Hampton, Virginia
C. Wellemeyer	ST Systems Corporation, Lanham, Maryland
J. Zawodny	NASA/Langley Research Center, Hampton, Virginia

Chapter 6 Trends in Stratospheric Temperature

M. Schoeberl, Chair, NASA/Goddard Space Flight Center, Greenbelt, Maryland

J. Angell	NOAA, Rockville, Maryland
J. Barnett	Oxford University, Oxford, England
B. Boville	NCAR, Boulder, Colorado
S. Chandra	NASA/Goddard Space Flight Center, Greenbelt, Maryland
S. Fels	NOAA, Geophysical Fluid Dynamics Laboratory, Princeton, New Jersey
E. Fleming	ARC Corporation, Landover, Maryland
M. Gelman	NOAA/NWS/Climate Analysis Center, Washington, D.C.
K. Labitzke	Free University of Berlin, Federal Republic of Germany
A.J. Miller	NOAA/NWS/Climate Analysis Center, Washington, D.C.
J. Nash	British Meteorological Office, England
P.A. Newman	NASA/Goddard Space Flight Center, Greenbelt, Maryland
V. Ramaswamy	Princeton University, Princeton, New Jersey

CONTRIBUTORS

J. Rosenfield NASA/Goddard Space Flight Center, Greenbelt, Maryland
F. Schmidlin NASA, Wallops Island, Virginia
M. Schwarzkopf NOAA, Geophysical Fluid Dynamics Laboratory, Princeton,
New Jersey
K. Shine Oxford University, Oxford, England

Chapter 7 Theory and Observations

I.S.A. Isaksen, Chair, University of Oslo, Oslo, Norway

R. Eckman University of Cambridge, Cambridge, England
A. Lacis Goddard Institute for Space Studies, New York, New York
M. Ko AER, Inc., Cambridge, Massachusetts
M. Prather Goddard Institute for Space Studies, New York, New York
J. Pyle University of Cambridge, Cambridge, England
H. Rodhe University of Stockholm, Stockholm, Sweden
F. Stordal University of Oslo, Oslo, Norway
R. Stolarski NASA/Goddard Space Flight Center, Greenbelt, Maryland
R. Turco R&D Associates, Marina del Rey, California
D. Wuebbles Lawrence Livermore National Laboratories, Livermore, California

Chapter 8 Trends in Source Gases

D. Ehhalt, Chair, Institute for Chemistry, Julich, Federal Republic of Germany
P. Fraser, Cochair, CSIRO, Aspendale, Australia

D. Albritton NOAA, Boulder, Colorado
R.J. Cicerone NCAR, Boulder, Colorado
M.A.K. Khalil Oregon Graduate Center, Beaverton, Oregon
M. Legrand CNRS, France
Y. Makide University of Tokyo, Japan
F.S. Rowland University of California, Irvine
L.P. Steele CIRES, University of Colorado/NOAA, Boulder, Colorado
R. Zander University of Liege, Liege-Ougree, Belgium

Chapter 9 Trends in Stratospheric Minor Constituents

R. Stolarski, Chair, NASA/Goddard Space Flight Center, Greenbelt, Maryland

W.P. Chu NASA/Langley Research Center, Hampton, Virginia
M.T. Coffey NCAR, Boulder, Colorado
W.S. Heaps NASA/Goddard Space Flight Center, Greenbelt, Maryland
J.A. Kaye NASA/Goddard Space Flight Center, Greenbelt, Maryland
M.P. McCormick NASA/Langley Research Center, Hampton, Virginia
R. Zander University of Liege, Liege-Ougree, Belgium

Chapter 10 Trends in Aerosol Abundances and Distributions

R.P. Turco, Chair, R & D Associates, Marina del Rey, California
 M.P. McCormick, Cochair, NASA/Langley Research Center, Hampton, Virginia

R.T. Clancy	LASP, University of Colorado, Boulder
R. Curran	NASA Headquarters, Washington, D.C.
J. DeLuisi	NOAA/ERL, Boulder, Colorado
P. Hamill	San Jose State University, San Jose, California
G. Kent	STC, Hampton, Virginia
J.M. Rosen	University of Wyoming, Laramie
O.B. Toon	NASA/Ames, Moffett Field, California
G. Yue	NASA/Langley Research Center, Hampton, Virginia

Chapter 11 Observations and Theories Related to Antarctic Ozone Changes

D. Hartmann, Cochair, University of Washington, Seattle, Washington
 R.T. Watson, Cochair, NASA Headquarters, Washington, D.C.

R.A. Cox	AERE, Harwell, England
C. Kolb	Aerodyne, Billerica, Massachusetts
J. Mahlman	NOAA, Geophysical Fluid Dynamics Laboratory, Princeton, New Jersey
M. McElroy	Harvard University, Cambridge, Massachusetts
A. Plumb	CSIRO, Aspendale, Australia
V. Ramanathan	University of Chicago, Chicago, Illinois
M. Schoeberl	NASA/Goddard Space Flight Center, Greenbelt, Maryland
S. Solomon	NOAA, Boulder, Colorado
R. Stolarski	NASA/Goddard Space Flight Center, Greenbelt, Maryland
N.D. Sze	AER, Inc., Cambridge, Massachusetts
A. Tuck	NOAA, Boulder, Colorado

Appendix A: Statistical Approaches to Ozone Trend Detection

P. Bloomfield, Chair, North Carolina State University, Raleigh

D.R. Brillinger	University of California, Berkeley
D. Nychka	North Carolina State University, Raleigh
R. Stolarski	NASA/Goddard Space Flight Center, Greenbelt, Maryland

CONTRIBUTORS

Acknowledgments

S. Chandra, Proofreading; Research Assistance—References	NASA/Goddard Space Flight Center, Greenbelt, MD
E. Fleming, Proofreading; Research Assistance—References	NASA/Goddard Space Flight Center, Greenbelt, MD
R.F. Hampson, Proofreading; Research Assistance—References	National Institute of Standards and Technology, Gaithersburg, MD
J.L. Hostetter, Research Assistance—References	ARC Professional Services Group, Washington, DC
C. Jackman, Proofreader; Research Assistance—References	NASA/Goddard Space Flight Center, Greenbelt, MD
J. Lynch, Proofreading	ST Systems Corporation, Lanham, MD
J. Lund, Typesetting	Systems Publications, Inc., Hyattsville, MD
R. Mills, Editorial Supervision and References	ST Systems Corporation, Lanham, MD
M. Tarlton, Jr., Graphics and Design	ST Systems Corporation, Lanham, MD
V. Vahlberg, Research Assistance—References	ST Systems Corporation, Lanham, MD
C. Wheel, Proofreading	ST Systems Corporation, Lanham, MD

APPENDIX C

Ozone Trends Panel Working Group Meetings

PRECEDING PAGE BLANK NOT FILMED

Appendix C

Ozone Trends Panel Working Group Meetings

Date	Meeting and Place	Chair
12/15-16, 1986	OZONE TRENDS PANEL NASA/GSFC, Greenbelt, MD	R.T. Watson
1/21, 1987	Data Intercomparisons Satellite-Satellite— Preliminary Meeting NASA/LaRC, Hampton, VA	H. Johnston
2/12-13	Algorithms Boulder, CO	C. Rodgers
2/19-20	Calibrations Instrument Performance NASA/GSFC, Greenbelt, MD	J. Gille
3/9-10	Data Intercomparisons S-S NASA/LaRC, Hampton, VA	H. Johnston
3/12-13	Dobson-Umkehr Intercomparisons Newport Beach, CA	F.S. Rowland
3/19-20	Calibrations Instrument Performance NASA/GSFC, Greenbelt, MD	J. Gille
3/23-24	OZONE TRENDS PANEL Boulder, CO	R.T. Watson
4/14-15	Algorithms LASP, Boulder, CO	C. Rodgers
5/4-5	Other Trends in Stratosphere— Preliminary Meeting NASA/LaRC, Hampton, VA	R. Stolarski
5/12-13	Dobson-Umkehr S-Ground Intercomparisons Atmospheric Environment Service Downsview, Ontario, Canada	F.S. Rowland
5/17	Satellite-Satellite Intercomparisons NASA/GSFC, Greenbelt, MD	H. Johnston
5/21-22	Theory and Observations Oslo, Norway	I. Isaksen
5/21-22	Calibrations Instrument Performance Johns Hopkins University Baltimore, MD	J. Gille

WORKING GROUP MEETINGS

5/25	Aerosols Marine del Rey, CA	R. Turco
6/18-19	OZONE TRENDS PANEL NASA/GSFC, Greenbelt, MD	R.T. Watson
6/23-25	Antarctic Ozone Symposium/WS NASA/Ames, Moffett Field, CA	R.T. Watson D. Hartmann
7/8-9	Temperature NASA/GSFC, Greenbelt, MD	M. Schoeberl
7/20	Aerosols Boulder, CO	R. Turco
7/20-21	Statistics Raleigh, NC	P. Bloomfield
7/27-28	Calibrations Boulder, CO	J. Gille
7/30-31	Dobson-Umkehr Intercomparisons Newport Beach, CA	F.S. Rowland
8/22	Theory and Observations Oslo, Norway	I. Isaksen
8/29	Source Gases Petersborough, Canada	D. Ehhalt
9/9-10	Satellite-Satellite Intercomparisons Oakland, CA	H.S. Johnston
9/14-16	Algorithms Somers Point, NJ	C. Rodgers
9/15-17	Theory and Observations Oslo, Norway	I. Isaksen
9/21-23	Calibrations Boulder, CO	J. Gille
9/30	Dobson-Umkehr Intercomparisons NASA/GSFC, Greenbelt, MD	F.S. Rowland
10/1-2	OZONE TRENDS PANEL NASA/GSFC, Greenbelt, MD	R.T. Watson
10/14-15	Temperature NASA/GSFC, Greenbelt, MD	M. Schoeberl
10/15	Source Gases Europe	D. Ehhalt

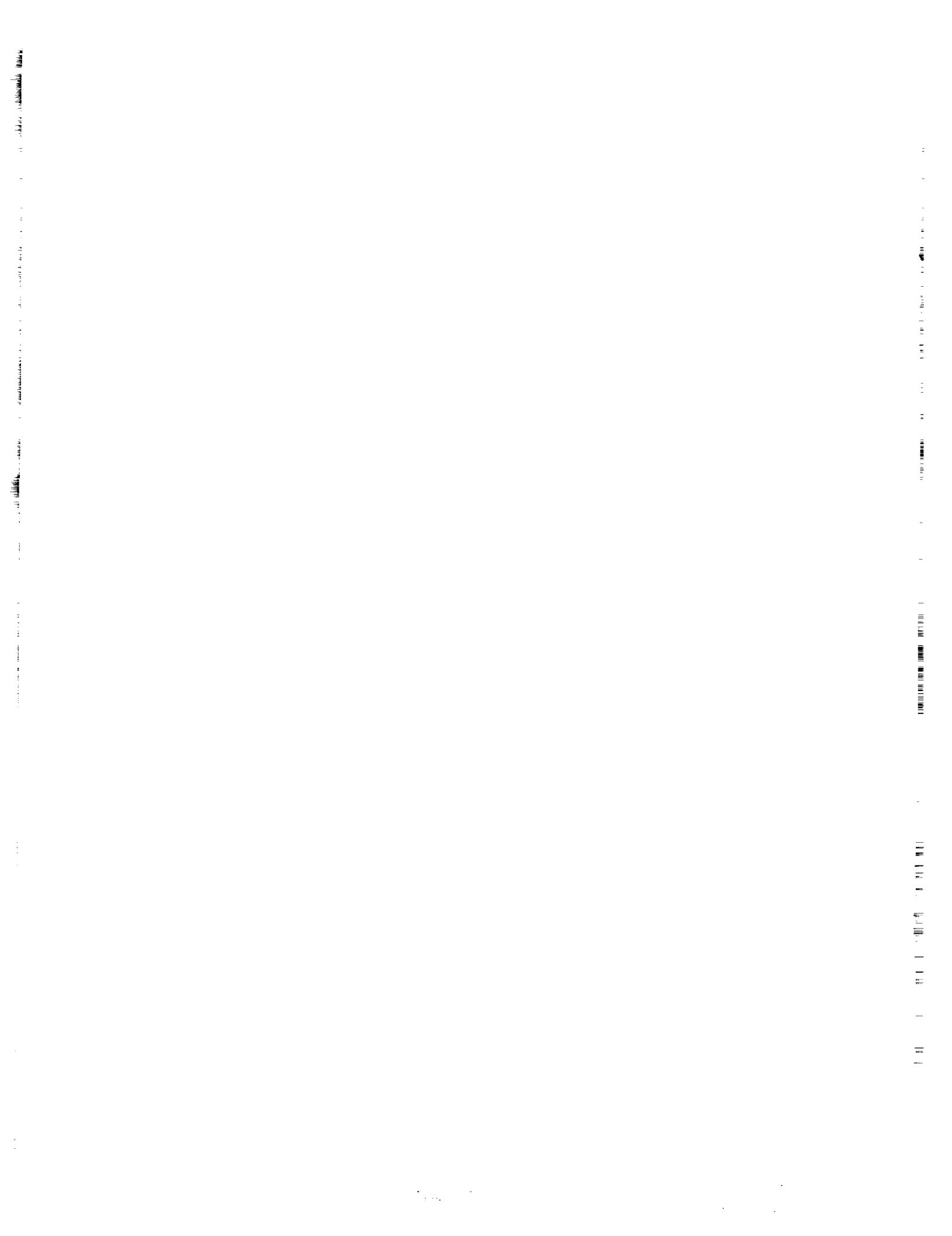
WORKING GROUP MEETINGS

11/9-11/13	OZONE TRENDS PANEL Editorial and Peer Review Meeting St. Croix, Switzerland	R.T. Watson
1/27-29, 1988	OZONE TRENDS PANEL and Peer Reviewers	R.T. Watson
March	Chapter Summaries Completed	All
3/15	Executive Summary of Ozone Trends Panel Released	
June	Extended chapter summaries received for <i>NASA Reference Publication 1208, Present State of Knowledge of the Upper Atmosphere 1988: An Assessment Report</i>	
August	<i>NASA RP 1208</i> Published	
October 1989	Preparation of <i>Report of the International Ozone Trends Panel—1988, Report No. 18, World Meteorological Organization Global Ozone Research and Monitoring Project</i>	



APPENDIX D

List of Figures



Appendix D

List of Figures

Figure 2.1	Periods of available data for satellite ozone-measuring systems.	12
Figure 2.2	Reflectivity as a function of wavelength for uncoated aluminum surfaces, one of which was exposed to an oil-pumped vacuum system, and the other (control sample) not.	13
Figure 2.3	Effect of UV irradiation on evaporated DC 705 oil. The effective layer thickness is $\cong 200\text{\AA}$, evaporated onto an aluminum surface coated with MgF_2 (enlarged 700 times).	14
Figure 2.4	Mass accumulation as a function of time in orbit for illuminated and shadowed quartz microbalances on the SCATHA spacecraft.	14
Figure 2.5	Bond energy of likely breaks of methyl phenyl siloxane (silicone rubber).	15
Figure 2.6	Reflectance at 270 nm of an uncoated oxidized aluminum plate as a function of the thickness of a carbon film deposited on its surface.	15
Figure 2.7	Schematic diagram of the SBUV instrument.	19
Figure 2.8a	The measured degradation of the SBUV instrument, $F_m(t)/F_m(0)$, for 1978–1987.	21
Figure 2.8b	The same as for Figure 2.8a, except for the six longest wavelengths.	21
Figure 2.9	Values of $r(\lambda)$ determined during the four frequent deployment periods by CPH.	27
Figure 2.10	Values of $S(\lambda)$ determined during the four frequent deployment periods by CPH.	28
Figure 2.11a	Percent difference between solar observation data and models.	30
Figure 2.11b	As in 2.11a, but for the six longest wavelengths.	30
Figure 2.12	Comparison at 340 nm between the measured solar irradiance, irradiance corrected for diffuser degradation, Earth radiance from 20°N – 20°S , and albedo, as a function of time.	32
Figure 2.13a	Relative diffuser reflectivity as a function of time for the OPT (CPH) and quasi-linear models, for the six shortest wavelengths.	35
Figure 2.13b	As in 13a, but for the six longest wavelengths.	35
Figure 2.14a	Relative spectrometer degradation as a function of time for the OPT (CPH) and quasi-linear models, for the six shortest wavelengths.	36
Figure 2.14b	As in 14a, but for the six longest wavelengths.	36
Figure 2.15a	The percent difference in the calculated albedo between the quasi-linear models and the exponential (CPH) fits for the six shortest wavelengths.	37
Figure 2.15b	The same as 15a, but for the six longest wavelengths.	37
Figure 2.16	Geometry of the earthshine observations.	39
Figure 2.17	Example of ratio of earthshine signal to direct solar irradiance as a function of subsatellite latitude.	39
Figure 2.18a	Comparison of diffuser reflectivity relative to 1978 versus wavelength, determined from earthshine measurements, and given by the models, for December 1983.	40
Figure 2.18b	As in 18a, but for December 1984.	40
Figure 2.18c	As in 18a, but for December 1985.	40
Figure 2.19	Wavelength pairs for total ozone determination.	41

FIGURES

Figure 2.20	Archived SBUV total ozone minus total ozone determined from SBUV D-pair wavelengths, 1980–1987 (from Bhartia, unpublished).	42
Figure 2.21	Uncertainty in ozone change determined from SBUV data over 8 years.	43
Figure 2.22	Uncertainty in rate of ozone change determined from SBUV data over 8 years.	44
Figure 2.23	Midlatitude vertical distributions of ozone change from 1978–1986 determined from SBUV data, for several models of diffuser degradation.	45
Figure 2.24	TOMS optical diagram.	47
Figure 2.25	Diagram of TOMS scanning swath.	48
Figure 2.26	Diffuser reflectivity vs. wavelength; comparison of model predictions for TOMS wavelengths.	51
Figure 2.27	SAGE–II sensor assembly.	54
Figure 2.28	SAGE–II spectrometer layout.	55
Figure 2.29	Data acquisition mode for solar extinction experiment during sunset event.	56
Figure 2.30	Sensitivity of ozone retrieval to variation of scan mirror reflectivity variation with angle.	58
Figure 2.31	Sensitivity of SAGE–II ozone retrieval to reference altitude errors (%/km), as a function of altitude.	59
Figure 2.32	Combined systematic errors in SAGE ozone profiles.	61
Figure 2.33	Uncertainty in SAGE ozone changes.	62
Figure 2.34	Uncertainty in ozone change determined from SAGE–I/SAGE–II differences.	64
Figure 2.35	SME orbit and scan geometry.	65
Figure 2.36	The geometry of limb viewing with the UVS on SME. Z_0 is the minimum ray height of the 3.5 km vertical resolution of the measurement.	67
Figure 2.37	Schematic drawing of the SME UV spectrophotometer.	68
Figure 2.38	(a) Random altitude-dependent errors associated with noise and data compression and temperature and pressure. (b) Systematic altitude-dependent errors associated with uncertainties in instrument sensitivity, instrument polarization, dead-time constants, and ozone cross-sections. (c) The altitude-dependent error from combined random and systematic errors.	69
Figure 2.39	(a) Example of IR horizon sensor trigger altitudes vs. latitude. (b) Altitude corrections vs. latitude.	71
Figure 2.40	NIR physical processes.	74
Figure 2.41	Optical scheme of the near-infrared spectrometer.	75
Figure 2.42	Normalized NIR photodiode sensitivity through the mission.	75
Figure 2.43	Total systematic error on ozone data estimated from input errors.	76
Figure 2.44	UV and NIR 0.75 mb mixing ratio with time. No correction for sensitivity drift of UV LW channel.	77
Figure 2.45	UV and NIR 0.75 mb mixing ratio with time. Correction for sensitivity drift of UV LW channel.	78
Figure 2.46	NIR 0.75 mb mixing ratio with time using the bus horizon sensors.	79
Figure 2.47	Ozone mixing ratios for June 1982–1986 for the UV instrument.	79
Figure 2.48	Schematic drawing of LIMS optical train.	82
Figure 2.49	Normalized instantaneous FOV functions for the six LIMS channels.	84
Figure 2.50	Normalized spectral response curves for LIMS channels.	85
Figure 2.51a	LIMS primary calibration curve for channel 3.	87
Figure 2.51b	Departure of curve in 2.51a from linearity.	87

Figure 2.52	LIMS detector temperature vs. time (expressed in orbit number). One week is approximately 100 orbits.	88
Figure 2.53	Percent variation of indicated scale factor around an orbit for LIMS carbon dioxide (temperature) and ozone channels.	89
Figure 2.54	(a) Scale factor for narrow CO ₂ channel as a function of time during LIMS missions. (b) Scale factor for wide CO ₂ channel as a function of time during LIMS missions. (c) Scale factor for wide O ₃ channel as a function of time during LIMS missions. (d) RMS noise in O ₃ channel as a function of time during LIMS missions.	90
Figure 2.55	Uncertainty in total change determined by the various experiments over their lifetimes, as functions of altitude. For SBUV, the uncertainty is half of the range between models of high and low diffuser degradation.	100
Figure 2.56	Uncertainties of trends determined by various experiments over their lifetimes, as functions of altitude. For SBUV, the uncertainty is half of the range between models of high and low diffuser degradation.	101
Figure 2.57	Midlatitude vertical distributions of ozone change from 1978–1986 determined from SBUV data, for several models of diffuser degradation. ...	102
Figure 3.1	Aerosol profile from SAGE-I: average ratio of aerosol to Rayleigh extinction at 292 nm, for 5°S in summer 1980.	127
Figure 3.2	Calculated SBUV spectral signature for the Figure 3.1 aerosol profile. .	128
Figure 3.3	The effect of the Fig. 3.1 aerosol on the SBUV-retrieved ozone profile.	129
Figure 3.4	SBUV averaging kernels for retrieved layer amounts.	131
Figure 3.5	(a) rms error in the SBUV profile due to a 1 percent random error in D_λ . (b) increase in ozone due to an increase in D_λ of 1 percent at all wavelengths. (c) rms scale error due to a 2 percent random error in $r(\lambda)$, after 8 years' operation. (d) increase in ozone due to a 5 percent increase in $r(\lambda)$ at all wavelengths.	132
Figure 3.6	Change in ozone relative to the SBUV archived data, due to the diffuser degradation models M1, M2, and L, as defined in Chapter 2.	133
Figure 3.7	Sensitivity of the SBUV retrieved layer amounts to errors in the mean layer temperatures. The curves are labeled with the layer in which the temperature is perturbed and are offset by multiples of 0.05%/K for clarity. ...	133
Figure 3.8	Sensitivities of the SBUV-retrieved layer amounts to errors in (a) surface reflectivity (b) surface pressure (c) Rayleigh-scattering coefficient (d) ozone absorption coefficient.	134
Figure 3.9	Umkehr averaging kernels for retrieved layer amounts.	140
Figure 3.10	Sensitivity of the Umkehr retrieval to absorption coefficient errors. ...	141
Figure 3.11	Changes in Umkehr retrievals due to the following absorption coefficient assumptions: (a) changing the coefficient ratio to the Bass–Paur value, keeping the difference unchanged. (b) Bass–Paur values at -44°C. (c) Bass–Paur values, including temperature dependence.	142
Figure 3.12	Sensitivity of Umkehr-retrieved ozone to atmospheric temperature changes. The curves are labeled with the number of the layer in which the temperature is perturbed by 20K and are offset by 1%/20K for clarity. .	143
Figure 3.13	Sensitivity of Umkehr-retrieved ozone to Rayleigh-scattering coefficient errors.	144
Figure 3.14	Sensitivity of the Umkehr-retrieved profile to errors in the total ozone measurement.	144

FIGURES

Figure 3.15	Sensitivity of the Umkehr-retrieved profile to surface reflectivity errors.	145
Figure 3.16	Effect on the ozone profile of changing the method of calculating the multiple-scattering correction.	146
Figure 3.17	Sensitivity of the Umkehr-retrieved profile to SO ₂ in the lower half of layer 1.	146
Figure 3.18	Averaging kernels for SAGE-II. Curves are not plotted for all altitudes.	152
Figure 3.19	Random error of a single SAGE-II profile due to instrument noise only.	153
Figure 3.20	Sensitivity of the SAGE retrieval to altitude reference error.	153
Figure 3.21	Sensitivity of SAGE retrieval to atmospheric temperature errors. Curves are labeled with the pressure level (mb) at which the NMC temperature is perturbed and are offset by multiples of 0.1%/K for clarity.	154
Figure 3.22	Averaging kernels for SME-NIRS at selected altitudes. (a) Slit tilt = 0°. (b) Slit tilt = 10°. (c) Slit tilt = 25°. Curves are labeled (1) 0.001 mb, (2) 0.0032 mb, (3) 0.01 mb, (4) 0.032 mb, (5) 0.1 mb, (6) 0.316 mb, and (7) 1 mb.	163
Figure 3.23	SME-NIRS sensitivities to model parameters at slit tilt = 0°. Units are percent ozone per percent parameter, except where stated. (a) $J_{3,\lambda}$ (b) τ_{UV} (c) τ_{762} (d) $\tau_{1.27}$ (e) $J_{S,\lambda}$ (f) A_s (g) A_D (h) k_D (i) k_N (j) k_O (k) k_s (l) Cal (m) Altitude reference (percent ozone per 0.01 km) (o) Solar zenith angle (percent ozone per 0.01 radian).	164
Figure 3.24	Sensitivity of SME-NIRS retrievals to temperature errors. (a) Density on a height scale (b) Mixing ratio on a log pressure scale. Plotted are the perturbations in the profile due to a 1K temperature change at (1) 90 km, (2) 82 km, (3) 74 km, (4) 66 km, (5) 58 km, and (6) 50 km.	165
Figure 3.25	LIMS ozone averaging kernels at three selected altitudes.	169
Figure 3.26	Sensitivity of LIMS-retrieved ozone to temperature errors at selected altitudes.	170
Figure 3.27	Sensitivity of LIMS-retrieved ozone to a 1K temperature change at all levels, a 1 percent radiance calibration error, and a 1 percent registration pressure error.	170
Figure 3.28	SBUV spectral signature for a Gaussian ozone depletion of 10 percent centered at 3 mb, with a width of 10 km at half maximum.	171
Figure 3.29	Umkehr measurement signature for a Gaussian-shaped depletion with a maximum of 25 percent and a half width of about 14 km centered at 3 mb (squares). Stratospheric aerosol signature (triangles). (a) Total ozone 200 DU. (b) Total ozone 300 DU. (c) Total ozone 400 DU.	173
Figure 4.1	Geographical distribution of Dobson stations with long records.	190
Figure 4.2	Total ozone monthly deviations at Mauna Loa (1957–1986). Calculated from the data published in <i>Ozone Data for the World</i> , showing the apparent disruption in the data in 1976–1977.	198
Figure 4.3	Geographical distribution of the M-83 filter ozonometers in the USSR (the numbers correspond to those given in Table 4.7).	200
Figure 4.4	The top panel shows the percentage difference between measurements of the Dobson Spectrophotometer and the TOMS instrument at Arosa, Switzerland. The middle and bottom panels show the actual measurements of the Dobson and the TOMS instruments, respectively.	206
Figure 4.5	Monthly mean biases (Dobson–TOMS)/Dobson and their respective intra-station standard deviations ($\pm 1\sigma$).	208

Figure 4.6	Monthly mean (Dobson-TOMS)/Dobson differences after the monthly biases have been removed. Stations where the σ of the monthly mean is less than 5 percent have not been included.	211
Figure 4.7	Fractional distribution of 71 Dobson stations and 21 M-83 filter stations according to the (station-TOMS)/station monthly mean differences in 1 percent intervals. More than two-thirds of the Dobsons, but only half of the M-83 stations, have less than 2 percent mean difference with the network average transferred via TOMS; 22 percent of all stations have differences ≥ 3 percent.	212
Figure 4.8	Fractional distribution of 92 stations according to the relative variability (σ in percent of the total ozone at a given station) of their monthly mean differences with TOMS.	213
Figure 4.9	Monthly differences between ozone measured at Huancayo and by TOMS (BR is bias removed), showing a slow upward drift during the first 4 years and a sharp decline in October 1982 (result of calibration). The σ of the differences forming each monthly point is about 2.6 percent.	214
Figure 4.10	Monthly (Dobson-TOMS)/Dobson differences for Bracknell indicating a downward rift between 1981 and 1984, followed by a sudden upward shift. The σ of the differences forming each monthly point is about 5.6 percent and is among the largest in the network.	215
Figure 4.11	Monthly (Dobson-TOMS)/Dobson differences for Singapore showing a strong downward drift between 1980-1983, when, as a result of calibration, the instrument is stabilized but at a level about 7 percent too low. The σ of differences forming each monthly point is about 2.4 percent. .	215
Figure 4.12	Monthly (Dobson-TOMS)/Dobson differences for Brisbane showing a downward drift until the end of 1980, followed by a sudden drop of about 5 percent. Only after calibration in early 1985 is the instrument restored to a state of agreement with the rest of the ozone network. The σ of the differences forming each monthly point is about 4.5 percent.	216
Figure 4.13	Monthly (Dobson-TOMS)/Dobson differences for Shiangher (near Beijing). The σ of the differences forming each monthly point is about 2.1 percent.	216
Figure 4.14	Monthly (Dobson-TOMS)/Dobson differences for Potsdam indicating a μ dependence as well as a shifting (in 1982-1983) of the level of ozone measured by the groundstation. The σ of the differences forming each monthly point is about 4.2 percent.	217
Figure 4.15	Monthly (Dobson-TOMS)/Dobson differences for Hobart showing an extremely large μ dependence and an erroneously low ozone level for the entire period of comparison. The σ of the differences forming each monthly point is about 4.7 percent.	218
Figure 4.16	Monthly (Dobson-TOMS)/Dobson differences for Hohenpeissenberg. The top panel indicates a well-pronounced μ dependence until 1985. The bottom panel shows the same monthly differences after removal of the μ -dependent variations and application of the instrument calibration procedures, indicating a very stable course, except too low by about 2.5 percent. This difference would be reduced by about 1 percent if an altitude correction is applied to the TOMS data. The σ of the differences forming each monthly point is about 2.8 percent, and is among the smallest in the network.	219

FIGURES

Figure 4.17	Monthly (Dobson–TOMS)/Dobson differences for Churchill indicating a constant difference of about 2.3 percent during most months, except for the winter (December and January are too low by about 7 and 5 percent, respectively). The σ of the differences forming each monthly point is about 5.1 percent.	220
Figure 4.18	Daily differences for Aarhus indicating extremely great scattering. The σ of the difference forming the monthly points (not plotted) is about 9.1 percent, the second largest in the network.	220
Figure 4.19	Daily differences for Toronto indicating stable direct-Sun readings (the σ of the differences of the monthly values is only about 2.2 percent) and very great scattering of the zenith-sky readings. The σ of the differences forming the monthly points from all observations (not plotted) is about 4.6 percent.	221
Figure 4.20	Comparison of the Belsk station-revised ozone data and the “fast” revised record, including corrections found during the August 1986 inter-comparisons. The data are plotted as monthly deviations that have been normalized and smoothed by taking the 12-month running mean.	222
Figure 4.21	The Belsk total ozone record as it was originally published in <i>Ozone Data for the World</i> . The data are plotted as normalized monthly ozone deviations that have been smoothed.	223
Figure 4.22	The 12-month running means of the total ozone measurements taken at Varanasi and New Delhi and recorded in <i>Ozone Data for the World</i>	224
Figure 4.23	The monthly total ozone deviations (a smooth plot of the actual deviation divided by the particular month’s interannual standard deviation) for Tateno and Kagoshima that are recorded in <i>ODW</i>	225
Figure 4.24	The monthly total ozone deviations (as in Figure 4.23) for Potsdam and Belsk. The Potsdam data are taken from <i>ODW</i> , and the Belsk data are the station-corrected set that was also published in <i>ODW</i> and that replaced the original values reported to <i>ODW</i>	225
Figure 4.25	The monthly deviations (as in Figure 4.23) for the originally published Belsk total ozone record and for the 100 mb temperature.	226
Figure 4.26	The monthly deviations (as in Figure 4.23) for the fast-revised Belsk total ozone record and for the 100 mb temperature.	227
Figure 4.27	The monthly deviations (as in Figure 4.23) for the station-revised Belsk total ozone record and for the 100 mb temperature. Since the station has, to date, revised the data only through December 1981, a provisional adjustment has been applied to the more recent data published in <i>ODW</i>	227
Figure 4.28	The monthly deviations (as in Figure 4.23) of the 100 mb temperature are plotted against the total ozone data from Churchill. In the upper panel, the ozone values published in <i>ODW</i> are shown, and in the lower panel the provisionally revised total ozone data set is plotted.	228
Figure 4.29	The provisionally revised total ozone data and the 100 mb temperatures for Bismarck are plotted.	229
Figure 4.30	Intercomparison of TOMS overpass measurements of total ozone with World Primary Standard Dobson ozone measurements at Mauna Loa Observatory, Hawaii, June 29, 1979.	234
Figure 4.31	The variation of the (TOMS minus Dobson) percentage difference with time given for three different types of Dobson measurements.	235
Figure 4.32	Average total ozone distribution for 1957–1975 derived from ground-based measurements.	237

Figure 4.33	Variation of total ozone with latitude and season.	238
Figure 4.34	Long-term means of the monthly total ozone values at Arosa, Switzerland, for August 1931–July 1986. The associated interannual standard deviations for each month are shown as ± 1 sigma vertical bars.	239
Figure 4.35	(a) Differences in the long-term monthly means at Arosa between August 1931–December 1969 and January 1970–July 1986. (b)–(f) Differences in the long-term monthly means at five other stations between the period prior to December 1975 and the period from January 1976 on.	240
Figure 4.36	Differences in the means of the 4-month “winter” season (DJFM) for the 11-year periods from January 1965–December 1975 and January 1976–December 1986 are plotted for 19 Northern Hemisphere stations. Data are taken from <i>ODW</i>	241
Figure 4.37	Differences in the means of the 4-month “summer” season (MJJA) for the 11-year periods from January 1965–December 1975 and January 1976–December 1986 are plotted for 19 Northern Hemisphere stations. Data are taken from <i>ODW</i>	242
Figure 4.38	Differences in the means of the 4-month “winter” season (DJFM) for the 11-year periods from January 1965–December 1975 and January 1976–December 1986 are plotted for 19 Northern Hemisphere stations. Provisionally revised data are used.	244
Figure 4.39	Differences in the means of the 4-month “summer” season (MJJA) for the 11-year periods from January 1965–December 1975 and January 1976–December 1986 are plotted for 19 Northern Hemisphere stations. Provisionally revised data are used.	244
Figure 4.40	Changes in monthly average ozone total amounts at Bismarck, North Dakota, between January 1963–December 1974 and January 1975–December 1986. Using (a) the data as published in <i>Ozone Data for the World</i> and (b) the provisionally revised data, with monthly average corrections for instrument calibrations applied to the data recorded in <i>Ozone Data for the World</i>	246
Figure 4.41	Description of trend (a) monotonic, year-round (hockey stick) and (b) separate hockey stick models for each calendar month.	252
Figure 4.42	Smoothed sunspot cycle 1957–1986	255
Figure 4.43	50 mbar Singapore wind speed, 1957–1986	256
Figure 4.44	Ozone decreases caused by the atmospheric nuclear bomb tests as calculated by the 2-D LLNL photochemical model for five different latitude bands.	256
Figure 4.45	Ozone changes for various stations between 1970 and 1986. The statistical model used allowed for effects of the solar cycle and the quasi-biennial oscillation, and data from 1965 (or when the station started making total ozone measurements if it did so after 1965) to 1986 were used. The ozone change in each month was assumed to have occurred in a linear fashion after 1969. The monthly ozone changes plotted are not trends; they are found by multiplying the calculated trend by the 17-year period over which the loss was assumed to have occurred. (a) Arosa, Switzerland, (b) Aspendale, Australia, (c) Belsk, Poland, (d) Bismarck, USA, (e) Boulder, USA, (f) Bracknell, UK, (g) Caribou, USA, (h) Edmonton, Canada, (i) Goose Bay, Canada, (j) Hohenpeissenberg, FRG, (k) Hradec Kralove, Czechoslovakia, (l) Leningrad, USSR, (m) Lerwick, UK, (n) Mauna Loa, USA, (o) Sapporo, Japan, (p) Tateno, Japan, (q) Toronto, Canada.	264 269

FIGURES

Figure 4.46	Phase of total ozone maximum.	270
Figure 4.47	Quasi-biennial oscillation of total ozone (Dobson Units—DU) in the mean values of Northern Hemisphere (NH), Southern Hemisphere (SH), globe (GL), and zonal mean values (ZM).	278
Figure 4.48	The calculated coefficients for the quasi-biennial term are plotted for 31 stations. At all latitudes except those between 30–39°N, the Singapore wind speed was kept concurrent with the total ozone (so that they are anticorrelated in northern latitudes). Between 30–39°N, a 6-month phase lag was imposed on the Singapore wind speed.	279
Figure 4.49	Variation of annual total ozone percentage deviations for the three latitude bands 53–64°N, 40–52°N, and 30–39°N. The most northerly band has the highest ozone values.	282
Figure 4.50	Variation of winter total ozone percentage deviations for the three latitude bands 53–64°N, 40–52°N, and 30–39°N.	283
Figure 4.51	Variation of summer total ozone percentage deviations for the three latitude bands 53–64°N, 40–52°N, and 30–39°N.	284
Figure 4.52	Ozone changes for the three latitude bands 53–64°N, 40–52°N, and 30–39°N between 1970 and 1986.	286
Figure 4.53	Annual total ozone cycles at Belsk and Bismark. The points represent the 10-day averages at each station calculated from 24 years of measure. . .	288
Figure 4.54	The points using the symbol ● are the differences in the monthly averages for the periods January 1963–December 1974 and January 1975–December 1986 for a combined series of the data from Belsk and Bismarck. The equivalent results when only Belsk was taken as operating in the former period are shown with the symbol □, while those for the case where just Bismarck was taken for the first period have the symbol ▲. In all cases, both stations' data were used in the second period.	289
Figure 4.55	The total ozone trends for the individual months are shown for the latitude band between 53°N and 64°N illustrating the effect of the addition of successive years of data.	292
Figure 4.56	The total ozone trends for the individual months are shown for the latitude band between 40°N and 52°N illustrating the effect of the addition of successive years of data.	293
Figure 4.57	The total ozone trends for the individual months are shown for the latitude band between 30°N and 39°N illustrating the effect of the addition of successive years of data.	294
Figure 4.58	Distribution of the changes between 1980 and 1986 in the 36 monthly trend coefficients for the three latitude bands shown in Figures 4.55, 4.56, and 4.57.	294
Figure 4.59	The total ozone trends for the individual months are shown for the latitude band between 53°N and 64°N illustrating the effect of the addition of successive years of data.	295
Figure 4.60	The total ozone trends for the individual months are shown for the latitude band between 40°N and 52°N illustrating the effect of the addition of successive years of data. The ozone change in each month was assumed to have occurred in proportion to the organochlorine burden of the troposphere, i.e., in a nonlinear fashion until the year shown, and the data used were from 1965 until the year shown. The statistical model used allowed for effects of the solar cycle and the quasi-biennial oscillation. The monthly ozone <i>trends</i> are given in DU/yr.	296

Figure 4.61 The total ozone trends for the individual months are shown for the latitude band between 30°N and 39°N illustrating the effect of the addition of successive years of data. 297

Figure 4.62 Distribution of the changes between 1980 and 1986 in the 36 monthly trend coefficients for the three latitude bands shown in Figures 4.59, 4.60, and 4.61. 297

Figure 4.63 Ozone changes for four regional averages composed from the USSR M-83 data taken between 1972 and 1986. 298

Figure 4.64 Variation of total ozone with latitude and season derived from TOMS measurements between 1979 and 1987. 299

Figure 4.65 Variation of total ozone with latitude and season derived from TOMS for each year from 1979 to 1987. 300

Figure 4.66 Globally averaged total ozone from November 1978–December 1987 derived from TOMS measurements. The solid line is a simple linear least squares fit of the data with a slope of $-0.4\% \text{ yr}^{-1}$ 301

Figure 4.67 (a) Deseasonalized global total ozone derived from TOMS. (b) Deseasonalized total ozone between 53°N and 53°S derived from TOMS. Percentage deviations from the seasonal means are plotted. 302

Figure 4.68 Zonal means of total ozone derived from TOMS for the areas between (a) 0–53°N and (b) 0–53°S. Percentage deviations from the seasonal means are plotted. 304

Figure 4.69 Zonal means of total ozone derived from TOMS for various latitude bands are plotted as percentage deviations from the weekly means. (a) 53–65°S, (b) 39–53°S, (c) 29–39°S, (d) 19–29°S, (e) 0–19°S, (f) 0–19°N, (g) 19–29°N, (h) 29–39°N, (i) 39–53°N, (j) 53–65°N. 305–306

Figure 4.70 Changes by month and latitude in total ozone between 1979–1980 and 1986–1987 as measured with TOMS on the Nimbus-7 satellite (2-year averages are used to minimize differences originating with the QBO). 307

Figure 4.71 (a-l) TOMS maps of monthly (January through December) total ozone change averaged from 1979 through 1987. 308–314

Figure 5.1 Global averages of SBUV ozone data for November 1978 to September 1984 using data between 70°S and 70°N with equal surface weighting, including Umkehr layers 6 to 9. 391

Figure 5.2 The SBUV weekly mean mixing ratios at 1.0 mb (about 50 km) for latitudes 10°N and 40°N. 392

Figure 5.3 The trend in SBUV ozone mixing ratio as a function of height for three periods, January 1979 to March 1982 (pre-El Chichón period), January 1979 to December 1984, and January 1979 to October 1986. For each period, the percentage change is computed using a least square fit of a time series containing the annual, semiannual, and linear trend terms. 392

Figure 5.4 The percentage change in ozone mixing ratio as a function of altitude and latitude from 1979–1986. The percentage change is computed for each pressure and latitude, as in Figure 5.3. 393

Figure 5.5 SAGE-I and SAGE-II yearly latitudinal coverage. 397

Figure 5.6 Cluster means of SAGE-I and SBUV at 40°S. 398

Figure 5.7 Cluster means of SAGE-I and SBUV at the Equator. 399

Figure 5.8 Cluster means of SAGE-I and SBUV at 40°N. 400

FIGURES

Figure 5.9	Cluster means of SAGE-II and SBUV at 40°S.	401
Figure 5.10	Cluster means of SAGE-II and SBUV at the Equator.	402
Figure 5.11	Cluster means of SAGE-II and SBUV at 40°N.	403
Figure 5.12	Time average of the cluster means. The averaging period for SAGE-I was October 24, 1979, to October 23, 1981. The averaging period for SAGE-II was October 24, 1984, to October 23, 1986. The corresponding SBUV data were similarly averaged.	404
Figure 5.13	The average of the percentage difference between SAGE-I and -II and SBUV cluster means with SBUV the reference. The averaging period was identical to that used for Figure 5.12.	405
Figure 5.14	Time averages of the percentage difference between SAGE-I and -II and SBUV cluster means with SBUV the reference. Averaging was done over all latitude bands for the time period used in Figure 5.12.	406
Figure 5.15	Averages of the percentage difference between the cluster means of SAGE-II and SAGE-I (SAGE-I the reference) or SBUV (1984-1986) and SBUV (1979-1981) (SBUV 1979-1981 the reference). Percentage differences were computed at SAGE-I and SAGE-II intersections. For each latitude band there were approximately eight intersections and thus eight percentage differences averaged to produce one point on the graph.	407
Figure 5.16	Latitudinally averaged mean percentage difference between SAGE-II and SAGE-I (SAGE-I the reference) or between SBUV (1984-1986) and SBUV (1979-1981) (SBUV 1979-1981 the reference).	408
Figure 5.17	Mean percentage difference between SAGE-II and SAGE-I at the geometric altitudes of SAGE (SAGE-I is the reference). For each latitude band approximately eight intersections were available from which to compute percentage differences. The average percentage difference along with its standard error are plotted. The standard error reflects only the variation between the eight percentage differences in a given latitude band.	409
Figure 5.18	Mean percentage difference between SAGE-II and SAGE-I at the geometric altitudes of SAGE (SAGE-I is the reference). All intersections occurring between 20°N to 50°N (or 20°S to 50°S) were combined into one sample. The percentage difference at each intersection was computed. These percentage differences were averaged and plotted for each altitude. The sample standard error was also computed and plotted as the horizontal bar at each point. Within each hemisphere, approximately 2,500 SAGE-I profiles and 6,000 SAGE-II profiles were used in computing the statistics.	410
Figure 5.19	Direct presentation of ozone observations (Dobson units) from the Umkehr station at Tateno (36°N) in the lower panel and collocated SBUV ozone observations in the upper panel from 1979 through 1986 for Umkehr layer 6.	413
Figure 5.20	Same as 5.19, except for Umkehr layer 7.	414
Figure 5.21	Same as 5.19, except for Umkehr layer 8.	415
Figure 5.22	Ratio of Umkehr ozone measurements in layer 8 to collocated SBUV measurements for 7 years after launching of SBUV in November 1978. Eleven Umkehr stations are included.	416
Figure 5.23	Aerosol-corrected Umkehr observations (Arosa, Belsk, Lisbon, and Tateno) plotted as a function of time in comparison with zonal average SAGE-II and SBUV data at 40°N latitude. This figure is a copy of Figure 5.11 with the Umkehr data added.	420

Figure 5.24	Plots of monthly average ozone concentration vs. time in Umkehr layer 6 for five Umkehr stations for precisely 7 years, including 1979 through 1986.	421
Figure 5.25	Same as 5.24, except it is for layer 7.	422
Figure 5.26	Same as 5.24, except it is for layer 8.	425
Figure 5.27	Comparison of zonal mean ozone layer amount calculated from the SBUV, SAGE-I, and LIMS observations for the case of March 1979 SAGE-I sunrise (Table 5.9).	428
Figure 5.28	Same as Figure 5.27 except for April 1979 SAGE-I sunset.	428
Figure 5.29	Percentage difference of zonal mean ozone layer amount of SBUV, SAGE-I, and LIMS from the average for the case of March 1979 SAGE-I sunrise (Table 5.9).	429
Figure 5.30	Same as Figure 5.29 except for April 1979 SAGE-I sunset.	430
Figure 5.31	SME UVS (+) and SBUV (*) average (0° to 60°N) mixing ratios at 1.0 mb for May, June, July, and August.	432
Figure 5.32	Envelope of maximum (2σ) trend of ozone mixing ratios from the UVS instrument of SME for June 1982 to 1986 at 0.75 mb. The error bars denote the range of the data (2σ) resulting from uncertainty in the determination of UVS sensitivity change with time.	433
Figure 5.33	Ozone concentration versus altitude for SMM (UVSP) and for SAGE-II.	434
Figure 5.34	Sunset ozone concentrations from the SMM instrument in the 53–57 km region plotted as a function of time for 20°N. Each point represents a weekly mean. The SBUV and SMM data were taken at different local times; at these altitudes, ozone changes during the diurnal cycle.	435
Figure 5.35	Same as Figure 5.34, except at 20°S.	435
Figure 5.36	Average ozone vertical profile based on ROCOZ-A and chemical ozone-sondes at Natal, Brazil, in March and April 1985. Middle panel: SAGE-II minus ROCOZ-A, vertical profile of ozone percentage difference at Natal in 1985 as a function of geometrical altitude. Right panel: SBUV minus ROCOZ-A, vertical profile of ozone percentage difference at Natal in 1985 at Umkehr layers and as a function of pressure.	440
Figure 6.1	Intercomparison of different radiosondes at night. a. Temperature differences from a standard defined by the U.S. and Finnish instruments. b. As in (a), but reported on standard pressure surfaces.	449
Figure 6.2	Weighting functions for satellite temperature instruments: a. MSU, SSU; b. Synthesized SSU channels.	451
Figure 6.3	Temperature changes in the 2 mb NMC analyses, as inferred from rocket comparisons, comparison of analyses around change dates, and regression, as explained in text.	456
Figure 6.4	Monthly 2 mb average temperature (a, unadjusted; b, adjusted to rocket; c, adjusted to joints) deviations from the long-term monthly averages for the Equator. Time runs from October 1978 (month 1) to April 1986 (month 91).	457
Figure 6.5	As in Figure 6.4, but for 30°N.	457
Figure 6.6	Temperature variation (K) in the 30–100 mb layer of “north temperate” latitudes, where a 1–2–1 weighting (1–1 at beginning and end of record) has been applied twice to successive seasonal deviations from the mean.	462
Figure 6.7	Seasonal temperatures with the long-term seasonal averages removed and smoothed 1–2–1 in time.	463

FIGURES

Figure 6.8	Seasonal temperatures with the long-term seasonal averages removed and smoothed 1–2–1 in time.	464
Figure 6.9	Seasonal temperatures with the long-term seasonal averages removed and smoothed 1–2–1 in time.	465
Figure 6.10	Seasonal temperatures with the long-term seasonal averages removed and smoothed 1–2–1 in time.	466
Figure 6.11	Seasonal temperatures with the long-term seasonal averages removed and smoothed 1–2–1 in time.	467
Figure 6.12	Seasonal temperatures with the long-term seasonal averages removed and smoothed 1–2–1 in time for SSU channel 47X centered at approximately 0.5 mb for a) Northern Hemisphere average, b) Southern Hemisphere average, c) global average, and d) 30°S–30°N average.	468
Figure 6.13	Seasonal temperatures with the long-term seasonal averages removed and smoothed 1–2–1 in time for the 30–35 km layer average of station rocket data and the corresponding zonal average of SSU channel 25 centered at approximately 15 mb for a) Ascension Island (9°S, 14°W), b) Cape Canaveral (28°N, 81°W), and c) Kwajalein (9°N, 168°E).	469
Figure 6.14	Seasonal temperatures with the long-term seasonal averages removed and smoothed 1–2–1 in time for the 30–35–40 km layer average of station rocket data and the corresponding zonal average of SSU channel 26 centered at approximately 6 mb.	470
Figure 6.15	Seasonal temperatures with the long-term seasonal averages removed and smoothed 1–2–1 in time for the 40–45–50 km layer average of station rocket data and the corresponding zonal average of SSU channel 27 centered at approximately 2 mb and SSU channel 36X centered at approximately 1.5 mb.	471
Figure 6.16	Seasonal temperatures with the long-term seasonal averages removed and smoothed 1–2–1 in time for the 50–55 km layer average of station rocket data and the corresponding zonal average of SSU channel 47X centered at approximately 0.5 mb.	471
Figure 6.17	Summary of global stratospheric temperature differences (1985 and 1986 minus the average of 1979 and 1980).	475
Figure 6.18	As in 6.17, except for Tropics and including rocket stations. Kwajalein Island (KI; 9°N, 168°E), Ascension Island (AI; 9°S, 14°W), and Cape Canaveral (CC; 28°N, 81°W).	475
Figure 6.19	1970–1986 linear regressions from Free University of Berlin data at 30 mb, and Angell and Korshover (1983a) climate zones from the 100–30 mb thicknesses.	476
Figure 6.20	Seasonal changes in tropospheric and stratospheric Northern Hemisphere temperature (degrees Celsius per 10 years) between 1973 and 1985 based on linear regression applied to rocketsonde data primarily in the Western Hemisphere (values above 25 km) and radiosonde data around the entire hemisphere.	477
Figure 6.21	Rocket observations for 30–55 km region at Ascension Island.	479
Figure 6.22	Same as 6.21 except for Kwajalein.	480
Figure 6.23	Same as 6.21 except for Barking Sands.	481
Figure 6.24	Same as 6.21 except for Cape Canaveral.	482
Figure 6.25	Same as 6.21 except for Pt. Mugu.	483
Figure 6.26	Same as 6.21 except for Primrose Lake.	484

Figure 6.27	Fractional decrease between 1979 and 1986 SBUV zonal mean monthly mean ozone mixing ratios.	486
Figure 6.28	Radiative equilibrium temperature differences computed by the three models for the June summer polar case. The differences plotted are computed using 1986 and 1979 ozone data.	487
Figure 6.29	As in Figure 6.28 except for the March equatorial case.	487
Figure 6.30	Radiative equilibrium computation for SAGE-observed ozone.	488
Figure 6.31	Changes in solar heating rates due to variations in the ultraviolet flux between solar minimum and solar maximum based on Heath and Schlesinger (1986) and Chapter 7 of this report. Units are degrees Kelvin per day.	489
Figure 6.32	Changes in radiative-convective equilibrium temperature due to changes in the solar ultraviolet flux over a solar cycle.	490
Figure 6.33	Effect of aerosols with an optical depth of 0.08 on a) solar heating rate, b) infrared heating rate, and c) temperature, for a tropical profile.	491
Figure 6.34	Changes in the net heating rate as a function of unimodal sulfate aerosol optical depth in a tropical atmosphere.	492
Figure 6.35	Aerosol-induced perturbations in radiative-convective equilibrium temperature as a function of unimodal sulfate aerosol optical depth.	493
Figure 7.1	Ozone-mixing ratio (ppmv) as a function of latitude and altitude for January from (a) LIMS and SBUV observations for 1979, (b) Calculations using Oslo 2-D model, (c) Calculations using AER 2-D model, (d) Calculations using Cambridge 2-D model, (e) Calculations using LLNL 2-D model.	514- 515
Figure 7.2	Altitude profile of ozone-mixing ratios for January in the Tropics from LIMS observations and the four 2-D models.	516
Figure 7.3	Total column ozone abundance (Dobson Units) as a function of latitude and season for (a) TOMS observations averaged 1979-1986, (b) Oslo, (c) AER, (d) Cambridge, and (e) LLNL models.	516- 517
Figure 7.4	Total odd nitrogen (NO_y in ppbv) as a function of latitude for summer from LIMS observations and from the four 2-D models for (a) 3 mb, (b) 16 mb, and (c) 30 mb. Also shown are results from ATMOS.	519
Figure 7.5	Altitude profiles of ClO mixing ratio for July, 30°N, from measurements and from four 2-D models.	520
Figure 7.6	Timeline of percent change in globally averaged column ozone from model calculations for the three cases described in Table 7.1: (1) trace gas emissions only, (2) trace gases plus solar cycle, and (3) trace gases, solar cycle, and atmospheric nuclear tests for the (a) Oslo, (b) AER, (c) Cambridge, and (d) LLNL models.	523
Figure 7.7	Calculated change (%) in column ozone changes as a function of time and latitude during the atmospheric nuclear tests. Results from the LLNL 2-D model are shown for 1962-1963.	524
Figure 7.8	Calculated change (%) in column ozone from 1979-1985 as a function of latitude and month from the Oslo model. The results demonstrate the effect of solar cycle (maximum to minimum) alone, neglecting all other influences.	525

FIGURES

Figure 7.9	Calculated change (%) in column ozone from 1979–1985 as a function of latitude and month, considering trace gases only (case 1). Calculations are from the (a) Oslo, (b) AER, and (c) LLNL models.	526
Figure 7.10	Timeline of percent change in column ozone from 1965 to 1985 for the latitude bands (a) 52–64°N, (b) 40–52°N, and (c) 30–40°N.	528
Figure 7.11	TOMS data for column ozone integrated from 65°S to 65°N are shown for 1978–1987. The TOMS satellite data have been normalized to the ground-based Dobson network.	529
Figure 7.12	Observed change (%) in column ozone from TOMS data, the average of 1985–1986 minus the average of 1979–1980. The TOMS data have been recalibrated and do not reflect the currently archived data: TOMS data for 1985 and 1986 have been increased by approximately 4 percent to account for drift with respect to Dobson network.	529
Figure 7.13	Calculated change (%) in column ozone as a function of latitude and season from 1979–1985, including effects of trace gases and solar cycle. Calculations are from the (a) Oslo, (b) AER, (c) Cambridge, and (d) LLNL models.	530
Figure 7.14	Observed change (%) in column ozone between the 11-year (solar-cycle) averages 1965–1975 and 1976–1986 for (a) summer season (May–June–July–August) and (b) winter season (December–January–February–March). Points representing values from single stations are plotted as a function of station latitude. Results from two 2-D models (Oslo and AER) are also shown.	531
Figure 7.15	Calculated height–latitude changes (%) in ozone from July 1979 to July 1985 for solar cycle only from the Oslo model (a), and solar cycle plus trace gases (case 2) from the (b) Oslo, (c) AER, (d) Cambridge, and (e) LLNL models.	533
Figure 7.16	Observed changes (%) in stratospheric ozone profiles from different instruments over 1979–1986. Differences between SAGE-I (1979–1980) and SAGE-II (1984–1985) measurements are shown for northern and southern latitudes (20°–50°). Umkehr observations from 1979–1986 are limited to northern midlatitudes.	535
Figure 7.17	Model calculations (Oslo) of globally averaged column ozone (Dobson Units) from 1979 extended to 1991 for the large and small solar-cycle variations.	538
Figure 8.1	Monthly mean mixing ratios of CCl ₃ F measured with HP5840 and HP5880 gas chromatographs on porosil columns at the ALE–GAGE stations between July 1978 and June 1986.	549
Figure 8.2	Monthly mean mixing ratios of CCl ₂ F ₂ measured with HP5840 and HP5880 gas chromatographs on porosil columns at the ALE–GAGE stations between July 1978 and June 1986.	550
Figure 8.3	Monthly mean mixing ratios of CH ₃ CCl ₃ measured with HP5840 and HP5880 gas chromatographs on silicone columns at the ALE–GAGE stations between July 1978 and June 1986.	551
Figure 8.4	Monthly mean mixing ratios of CCl ₄ measured with HP5840 and HP5880 gas chromatographs on silicone columns at the ALE–GAGE stations between July 1978 and June 1986.	552
Figure 8.5	Trends of atmospheric concentrations of CCl ₂ FCClF ₂ (CFC–113) observed in Hokkaido, Japan, and as a global average of six sampling sites.	556

Figure 8.6	The global distribution of $\text{CCl}_2\text{FCClF}_2$ in 1985 from six sampling sites (Barrow, Alaska; Cape Meares, Oregon; Mauna Loa, Hawaii; Cape Matatula, American Samoa; Cape Grim, Tasmania; South Pole).	556
Figure 8.7	Monthly mean CHClF_2 observations (pptv) at Cape Grim, Tasmania, from the Oregon Graduate Center flask sampling program.	557
Figure 8.8	Monthly mean CH_3Cl observations (pptv) at Cape Grim, Tasmania, from the Oregon Graduate Center flask sampling program.	557
Figure 8.9	Measured and predicted cumulative increases of chlorinated source gases in the troposphere over the past decade and up to 1990. The concentrations are given as chlorine atom equivalents.	558
Figure 8.10	Monthly mean concentrations of CBrF_3 and CBrClF_2 at Cape Meares, Oregon, over the last decade. Concentrations of CBrF_3 have increased exponentially at $18(\pm 1)$ percent/yr and linearly for CBrClF_2 at $0.12(\pm 0.01)$ pptv/yr.	559
Figure 8.11	Observations of CBrClF_2 (pptv) in the Southern Hemisphere at Cape Grim, Tasmania, and at the South Pole.	560
Figure 8.12	The monthly and globally averaged concentrations of N_2O based on ALE-GAGE data collected using in situ gas chromatographs at Adrigole, Cape Meares, Barbados, Samoa, and Cape Grim, and flask data from Barrow and Mauna Loa.	561
Figure 8.13	N_2O measurements obtained from ice cores.	561
Figure 8.14	Results from four long-term, methane measurement programs based upon gas chromatography and flame ionization detection: (a) the Commonwealth Scientific and Industrial Research Organisation, Australia (CSIRO); (b) the Geophysical Monitoring for Climate Change program of the National Oceanic and Atmospheric Administration (NOAA); (c) the Institute of Atmospheric Sciences, Oregon Graduate Center (OGC); and (d) the University of California at Irvine (UC).	563
Figure 8.15	Time series of monthly mean methane concentrations measured by flask sampling from aircraft in the mid-troposphere (3.5 to 5.5 km altitude) over the southeastern Australian region.	563
Figure 8.16	Zonally averaged representation of the variations in atmospheric methane concentrations in the remote marine boundary layer for the 4-year period May 1983 to April 1987.	564
Figure 8.17	Summary of methane concentrations measured in air bubbles extracted from ice cores in both Greenland and Antarctica. Data are from several investigations, and differing methods of extracting the air from the ice have been used.	565
Figure 8.18	Hemispheric and global averages of deseasonalized CO concentrations.	566
Figure 8.18	Hemispheric and global averages of deseasonalized CO concentrations.	566
Figure 8.19	Monthly mean CO observations in the Southern Hemisphere from Samoa, Cape Grim, Mawson, and the South Pole.	567
Figure 8.20	Nitrate (NO_3) trends over the last 100 years: (a) Dye 3, South Queensland, (b) South Pole, Antarctica.	568

FIGURES

Figure 9.1.	Solar occultation measurements of daytime mixing ratios of NO ₂ in ppbv by the SAGE and SAGE-II (preliminary data) instruments.	576
Figure 9.2.	NO ₂ column amounts above 12 km from a number of ground- and aircraft-based measurements.	578
Figure 9.3.	NO ₂ column amounts above 24 km from indicated satelliteborne experiments.	579
Figure 9.4.	Monthly averaged NO ₂ slant column amounts at Lauder, New Zealand (45°S, 170°E).	580
Figure 9.5.	SBUV NO data showing column amount of NO above 1 mb in molecules per cm ² as a function of time for the period 1979 to 1986 in the indicated latitude ranges.	581
Figure 9.6.	Plot of total odd nitrogen measured by ATMOS on 5/1/85, at 30°N, LIMS descending node NO ₂ + HNO ₃ , and LIMS descending node NO ₂ + HNO ₃ plus twice the N ₂ O ₅ inferred from a photochemical model.	583
Figure 9.7.	Time series plot of column amount of hydrogen chloride (HCl) measured from the ground, aircraft, or shuttle during the period 1976 to 1987. ..	584
Figure 9.8.	Time series plots of column amount of hydrogen fluoride (HF) measured from the ground, aircraft, or space during the period 1976 to 1987. ...	587
Figure 9.9.	Time series of midday ClO column abundances above 30 km measured by ground-based millimeter wave spectrometry taken from Hawaii.	588
Figure 9.10.	Time series of stratospheric H ₂ O vapor measurements made by frost-point hygrometer measurements. (a) 60 mb mixing ratios obtained from balloon flights launched at Washington, D.C. (1963 to 1980), and Boulder, Colorado (since 1980). (b) Representative stratospheric humidity measured on aircraft flights over southern England near 50°N from 1972 to 1980. (c) Mean 15 to 21 km water vapor mixing ratio (ppmm) over Mildura and Alice Springs, Australia, from 1973 to 1979.	590
Figure 9.11.	Time series of normalized monthly OH column amounts from indicated groundstations. (a) Fritz Peak, Colorado. (b) Boca Raton, Florida.	591
Figure 10.1	Geometries for ozone passive remote sensing. Configurations for both space-based and ground-based sensors are indicated.	606
Figure 10.2	Decrease in direct solar transmission due to aerosol turbidity (extinction) at Mauna Loa, Hawaii, from 1958 to 1986, based on broad-band solar pyrhelimeter measurements.	610
Figure 10.3	Integrated lidar backscatter intensities over the decade 1974 to 1985 for a wavelength 0.6943 μm at two sites: (a) Mauna Loa; (b) Hampton, VA. ..	612
Figure 10.3	Integrated lidar backscatter intensities over the decade 1974 to 1985 for a wavelength 0.6943 μm at two sites: (a) Mauna Loa; (b) Hampton, Virginia.	612
Figure 10.4	Simultaneously measured aerosol and ozone profiles over Minneapolis, Minnesota, on December 22, 1965.	613
Figure 10.5	Aerosol vertical profiles obtained with the six-channel dustsonde.	614
Figure 10.6	Time development of the peak mass mixing ratio of the stratospheric aerosol layer over Laramie, Wyoming, during the entire period of regular dustsonde operations at that site.	615

Figure 10.7	Optical depth of aerosols in the polar stratosphere at a wavelength of 1 micron measured by the SAM-II satellite from October 1978 through September 1986.	617
Figure 10.8	Global distribution of the aerosol optical depth (measured at a wavelength of 1 μm) roughly 2.5 months after the eruption of Mount St. Helens in May 1980.	618
Figure 10.9	Contours of inferred vertical and temporal variations in the aerosol extinction at a wavelength of 6.8 μm (given in units of 10^{-4} km^{-1} , with values indicated on the contours) from SME infrared radiometer data for the first year following the El Chichón eruption of April 4, 1982.	619
Figure 10.10	Contours of volume-scattering ratios at a wavelength of 440 nm from the SME visible spectrometer for observations at 40°N, the Equator, and 40°S, covering the period 1982 through mid-1986.	620
Figure 10.11	Time-longitude contours of SME visible-wavelength (440 nm) volume-scattering ratios at equatorial latitudes, for altitudes of 37.5 km and 30.5 km.	621
Figure 10.12	Comparison of extinction ratios (here, the ratio of aerosol extinction to molecular Rayleigh extinction, at a wavelength of 450 nm) from SAGE-II limb extinction measurements converted to extinction (volume scattering) using two distinct aerosol size distributions.	623
Figure 10.13	Balloonborne dustsonde measurements of the vertical concentration profile of particles with radii greater than 0.15 μm over Laramie, Wyoming.	627
Figure 10.14	Integrated lidar aerosol backscatter intensity (in units of 10^{-4} sr^{-1}) for the stratosphere (i.e., from the tropopause upward) versus latitude from an aircraft survey.	628
Figure 10.15	Perspective plot of the integrated stratospheric lidar backscatter intensity versus latitude for different times after the El Chichón eruption.	631
Figure 10.16	Time development of the global-average stratospheric aerosol optical depth, referred to the zenith, at a wavelength of 1 μm . Data were obtained from the SAGE and SAM-II satellite systems.	632
Figure 10.17	Illustration of the geometry for zenith Umkehr observations of scattered solar radiation, with the Sun at an elevation of 0°.	633
Figure 10.18	Normalized contribution functions (i.e., the relative vertical intensity profiles for primary scattered radiation, which are related to the weighting functions of Chapter 3) for the Umkehr C (311.4 and 332.4 nm) wavelength pair at several solar zenith angles.	634
Figure 10.19	Residual, or aerosol-induced, ΔN -values in the Umkehr C-pair measurement versus solar zenith angle for three aerosol fields.	635
Figure 10.20	Model profiles for aerosol concentration that have been used in ozone/aerosol Umkehr error calculations.	635
Figure 10.21	Errors in Umkehr ozone measurements resulting from stratospheric aerosol interference.	637
Figure 10.22	Monthly averaged midlatitude stratospheric aerosol optical depth (above 15 km) versus time, as compiled from lidar measurements at four sites in the United States, Wales, Germany, and France.	638
Figure 10.23	Illustration of the geometry for SBUV nadir observations of scattered solar radiation.	639
Figure 10.24	A polar stratospheric cloud extinction profile obtained from SAM-II data for January 23, 1979, at 68.7°N and 27°W.	642

FIGURES

Figure 10.25	Average aerosol extinction profile for January 1979 in the Northern Hemisphere. The data correspond to all of the SAM-II observations for that month.	643
Figure 10.26	Histogram showing the longitudinal distribution of PSC events in the Southern Hemisphere for the winters of 1979–1981 based on SAM-II observations.	645
Figure 10.27	Averaged altitude of the maximum aerosol (PSC) extinction (on the vertical profile of extinction) for SAM-II satellite measurements over Antarctica during 13 weeks of a winter season.	646
Figure 10.28	Frequency of cloud sightings by the SAM-II detector as a function of the minimum stratospheric temperature in the vicinity of the clouds, during the austral winter of 1981.	646
Figure 10.29	Detailed SAM-II extinction measurements at 50 mb over a 130-day period during the austral winter and spring of 1981.	647
Figure 10.30	An expanded plot of a segment of the data in Figure 10.29.	648
Figure 10.31	Temperature variations at 50 mb for the same period and geographical locations as in Figure 10.30.	648
Figure 10.32	Histograms of the statistical characteristics of the total ensemble of Southern Hemisphere PSC's having extinctions greater than 2×10^{-3} detected by the SAM-II satellite in 1986.	649
Figure 10.33	As in Figure 10.32, except for the PSC's observed in the Northern Hemisphere in 1986.	650
Figure 10.34	Extinction ratios at 18 km versus time as measured by the SAM-II system in the Southern Hemisphere (i.e., the total extinction including aerosol effects obtained by the satellite limb sensor, divided by the extinction caused by molecular Rayleigh scattering obtained from an atmospheric model; ratios that exceed unity are associated with aerosol extinction).	652
Figure 10.35	Relative frequency (in percent) of observed aerosol extinction ratios at 18 km for 1979 and 1985 through 1987 (as in Figures 10.34a–d) for two specific intervals: (a) September 10 to 20 and (b) September 20 to 30.	653
Figure 10.36	Freezing-point curves for nitric acid aqueous solutions as a function of the nitric acid weight percent of the solution at a pressure of 1 atmosphere.	655
Figure 10.37a	Vapor pressures of HNO_3 over aqueous solutions and ices of various compositions as a function of temperature ($1000/T$).	656
Figure 10.37b	Same as Figure 10.37a, except for the H_2O vapor pressures.	657
Figure 10.38	HNO_3 vapor pressures over aqueous HNO_3 solutions and solid phases.	658
Figure 10.39	Lidar backscatter ratio for a PSC at 90°N measured with the NASA/Langley airborne lidar system	660
Figure 11.1	October monthly mean total ozone measurements over Halley Bay. ...	670
Figure 11.2	Deviation of total ozone from seasonal mean over Argentine Islands, Syowa, Halley Bay, and South Pole stations from 1957 through 1986. .	671
Figure 11.3	TOMS maps of Southern Hemisphere, total ozone for Octobers from 1979 through 1987. Maps are polar orthographic projections with Equator at outside and South Pole at center.	672
Figure 11.4	Polar orthographic maps of TOMS October mean Southern Hemisphere total ozone for (a) odd years and (b) even years.	673
Figure 11.5	Polar orthographic maps of TOMS September mean Southern Hemisphere total ozone for (a) odd years and (b) even years.	674

Figure 11.6	Daily zonal mean TOMS total column ozone for latitude band $60^{\circ}\text{S} \pm 1^{\circ}$ from day 210 to day 280, yearly from 1984 to 1987, with 1979 as reference year, using normalized TOMS data (NTD).	675
Figure 11.7	Daily zonal mean TOMS total column ozone for latitude band $70^{\circ}\text{S} \pm 1^{\circ}$ from day 210 to day 280, yearly from 1984 to 1987, with 1979 as reference year, using normalized TOMS data (NTD).	677
Figure 11.8	Daily zonal mean TOMS total column ozone for latitude band $80^{\circ}\text{S} \pm 1^{\circ}$ from day 210 to day 280, yearly from 1984 to 1987, with 1979 as reference year, using normalized TOMS data (NTD).	677
Figure 11.9	Daily zonal mean TOMS total column ozone versus time of year at 60°S for the years 1979 through 1987.	678
Figure 11.10	Daily zonal mean TOMS total column ozone versus time of year at 70°S for the years 1979 through 1987.	679
Figure 11.11	Daily zonal mean TOMS total column ozone versus time of year at 80°S for the years 1979 through 1987.	679
Figure 11.12	Zonally averaged TOMS ozone plotted versus latitude for the month of September from 1979 through 1987.	680
Figure 11.13	Zonally averaged TOMS ozone plotted versus latitude for the month of October from 1979 through 1987.	680
Figure 11.14	Annual progression of TOMS total ozone integrated over the area from 90°S to 44°S plotted for each year from 1979 through 1987.	681
Figure 11.15	Progression of TOMS total ozone integrated over the area from 44°S to 90°S from August through October plotted for each year from 1979 through 1987 (normalized TOMS data used).	682
Figure 11.16	Difference between recent 2 years (1986–1987) of TOMS total ozone measurements and first 2 years (1979–1980) as a function of latitude and season. Two years are used to approximately remove the quasi-biennial oscillation.	682
Figure 11.17	Daily TOMS maps of total column ozone in the Southern Hemisphere for October 15, November 15, November 29, and December 5, 1987 (polar orthographic projection).	683
Figure 11.18	TOMS maps of total column ozone in the Southern Hemisphere for August 17, September 5, September 27, and October 5, 1987.	684
Figure 11.19	TOMS maps of total column ozone in the Southern Hemisphere for September 3–6, 1987.	685
Figure 11.20	Vertical distribution of ozone over Syowa measured by ozonesonde from July through November.	686
Figure 11.21	Ozone partial pressure as function of altitude over McMurdo as measured by ozonesonde. Shown are August 28 and October 16, 1986.	687
Figure 11.22	Ozone profiles over South Pole measured by ozonesonde for August 9 and October 7, 1986.	688
Figure 11.23	Vertical distribution of the ozone partial pressure (nbar) observed at Halley Bay Station on August 15, 1987 (high values), and October 15, 1987 (low values), respectively.	688
Figure 11.24	(a) Ozone partial pressure over Palmer station on October 6 and 9, 1987; (b) temperature profile for October 6 and 9, 1987, over Palmer Station.	689
Figure 11.25	Ozone partial pressure over McMurdo measured by ozonesonde; (a) comparison of August 29, 1987, to October 6, 1987, and (b) comparison of August 29, 1987, to November 5, 1987.	690

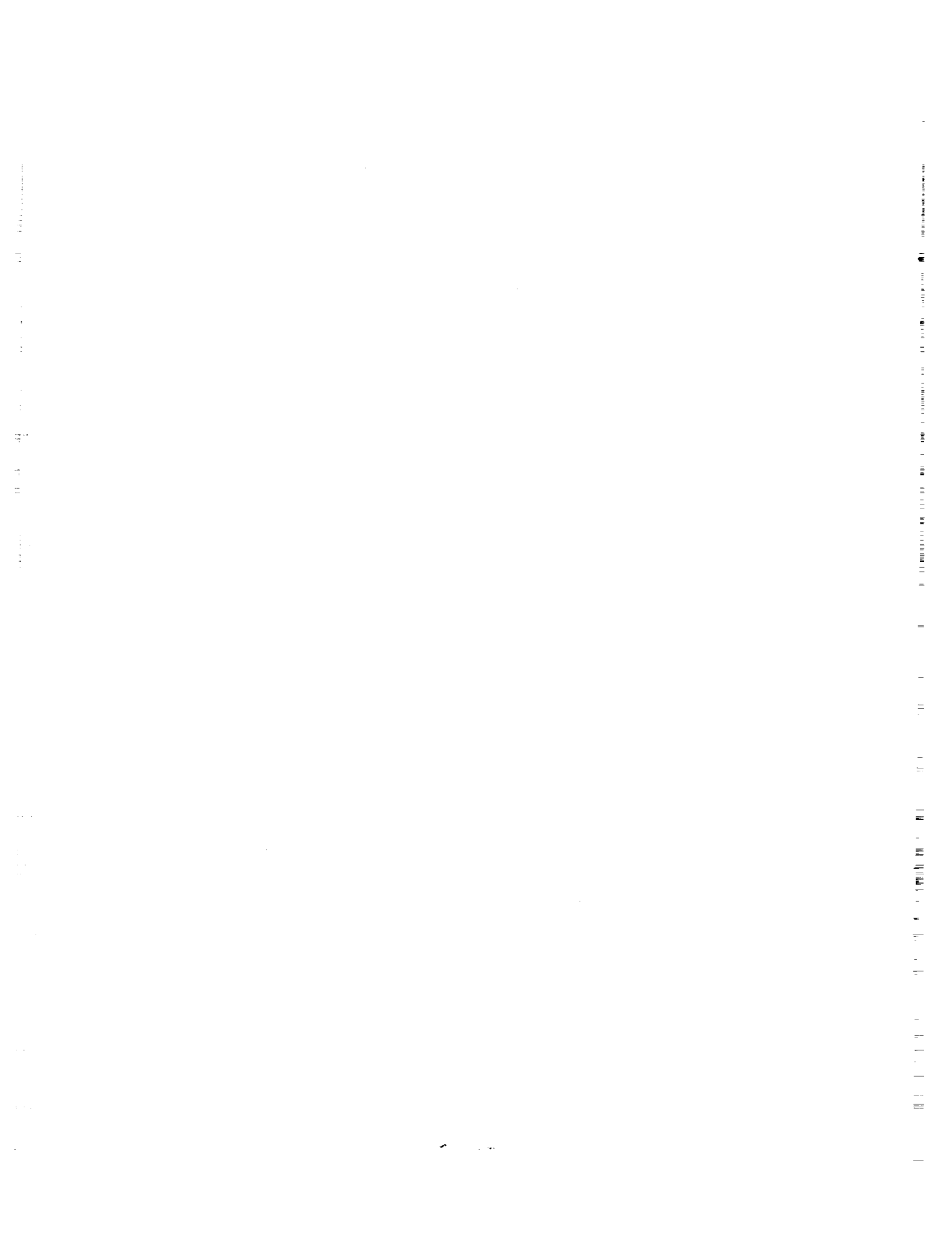
FIGURES

Figure 11.26	Comparison of ozone profiles measured by SAGE with Halley Bay ozone-sondes for October 7, 1987.	690
Figure 11.27	Ozone-sonde partial pressure measurements for several days over McMurdo during 1986.	691
Figure 11.28	SAM-II weekly averaged stratospheric optical depth at 1 μm over the Arctic and Antarctic regions from October 1978 to September 1986. ...	692
Figure 11.29	Contour plots of SAM-II weekly averaged extinction ratio at 1 μm for (a) 1980, (b) 1982, (c) 1984.	693
Figure 11.30	SAM-II extinction ratios versus time of year for (a) 1979 at 18 km altitude, (b) 1987 at 18 km altitude, (c) 1979 at 20 km altitude, (d) 1987 at 20 km altitude.	694
Figure 11.31	Time series of October mean 100 mb (100hPa) temperatures over eight Antarctic stations. Data from 1957–1984 are from rawinsonde observations (RAOB) and data from 1979–1986 are from NMC analyses.	696
Figure 11.32	Time series of October mean 30 mb (30hPa) temperatures over eight Antarctic stations. Data from 1957–1984 are from rawinsonde observations (RAOB) and data from 1979–1986 are from NMC analyses.	697
Figure 11.33	October 1983 maps of (a) temperature at 100 mb (hPa), (b) temperature at 30 mb (hPa), and (c) TOMS total ozone.	698
Figure 11.34	Time series of November mean 100 mb (100hPa) temperatures over seven Antarctic stations. Data from 1957–1984 are from rawinsonde observations (RAOB) and data from 1979–1986 are from NMC analyses.	699
Figure 11.35	NMC 1979–1986 zonal mean temperature averages (top, $^{\circ}\text{K}$) and 1979–1986 trends (bottom, $^{\circ}\text{K}/\text{yr}$) for August, September, October, and November.	700
Figure 11.36	NMC temperature differences between 1979–1983 at (a) 100hPa and (b) 30hPa, with RAOB differences superimposed in bold type. The bottom figure shows the TOMS total ozone difference.	701
Figure 11.37	Year-to-year change of monthly total ozone amount and 100hPa temperature at Syowa Station: (a) October, (b) November, and (c) December. .	702
Figure 11.38	Smoothed seasonal temperature deviations at 100, 50, and 30hPa above Antarctica compared with smoothed seasonal total ozone deviations in Antarctica.	703
Figure 11.39	Latitude–time contour plots of the annual variation of zonal mean total ozone from Dobson stations before 1974.	705
Figure 11.40	TOMS satellite data versus latitude and season between 1979–1982. ...	706
Figure 11.41	Five-year mean climatology of zonal mean temperature (K) for (a) July in the Southern Hemisphere and (b) January in the Northern Hemisphere, and of zonal mean wind (m/s) for c) October in the Southern Hemisphere and d) April in the Northern Hemisphere.	709
Figure 11.42	(a) October NMC 70 mb temperature trend from 1979 to 1985 and (b) TOMS total ozone trend over the same period.	714
Figure 11.43	Northward eddy heat flux calculated from NMC analyses and averaged over 1979–1985 (top, $^{\circ}\text{K m s}^{-1}$) and the trend in eddy heat flux (bottom, $^{\circ}\text{K m s}^{-1} \text{yr}^{-1}$) over the same period for August, September, and October.	715
Figure 11.44	Time–height contours of the ozone-mixing ratios used in the radiative heating calculations with depleted ozone. Contours are 0.5 ppmv.	717
Figure 11.45	Difference of radiatively determined temperatures for depleted and undepleted ozone computed from Model 1, from September 1 through September 30. Units are 0.5°K	718

Figure 11.46	Difference of radiatively determined temperatures for depleted and undepleted ozone computed from Model 2, from September 1 through September 30. Units are 0.5 °K.	718
Figure 11.47	Difference of radiatively determined temperatures for depleted and undepleted ozone computed from Model 3, from September 1 through September 30. Units are 0.5 °K.	719
Figure 11.48	The mean of 1985 and 1986 minus the mean of 1979 and 1980 NMC temperature profiles collocated with the total ozone minimum for September 1 to October 30. Units are 2.0 °K.	720
Figure 11.49	Maximum and minimum TOMS total ozone values south of 30°S, plotted as a function of day over the June–December period for each year between 1979 and 1987.	722
Figure 11.50	Evolution of the nonvolcanic particle size distribution at 70 mb with temperature. Shown are the size distributions at 195 K, 191 K, and 189 K, assuming a cooling rate of 0.5 K/day.	730
Figure 11.51	Ground-based mm-wave spectral data from McMurdo Station, taken in September 1986.	736
Figure 11.52	Observed trend in lower atmospheric ClO component over McMurdo Station during the period September 1–October 16, 1986.	737
Figure 11.53	Diurnal variation of integrated ClO emission line intensity measured at McMurdo Station in 1986.	737
Figure 11.54	OCIO vertical column over McMurdo from September 16–19, 1986, measured by direct moonlight.	738
Figure 11.55	OCIO vertical column over McMurdo from late August through mid-October 1986 measured during twilight. Also shown is the 50 mb temperature.	738
Figure 11.56	Vertical column abundances for the chlorine reservoir species HCl, ClONO ₂ , and their sum. The column abundance value for the HF obtained on October 12, 1986, is also shown.	741
Figure 11.57	NO ₂ vertical column over McMurdo from late August through mid-October, 1986, measured during evening twilight compared to 50 mb temperatures	741
Figure 11.58	Vertical column abundances of HNO ₃ , NO, and NO ₂ , over McMurdo Station during September and October 1986.	742
Figure 11.59	ClO mixing ration versus altitude.	745

Appendix

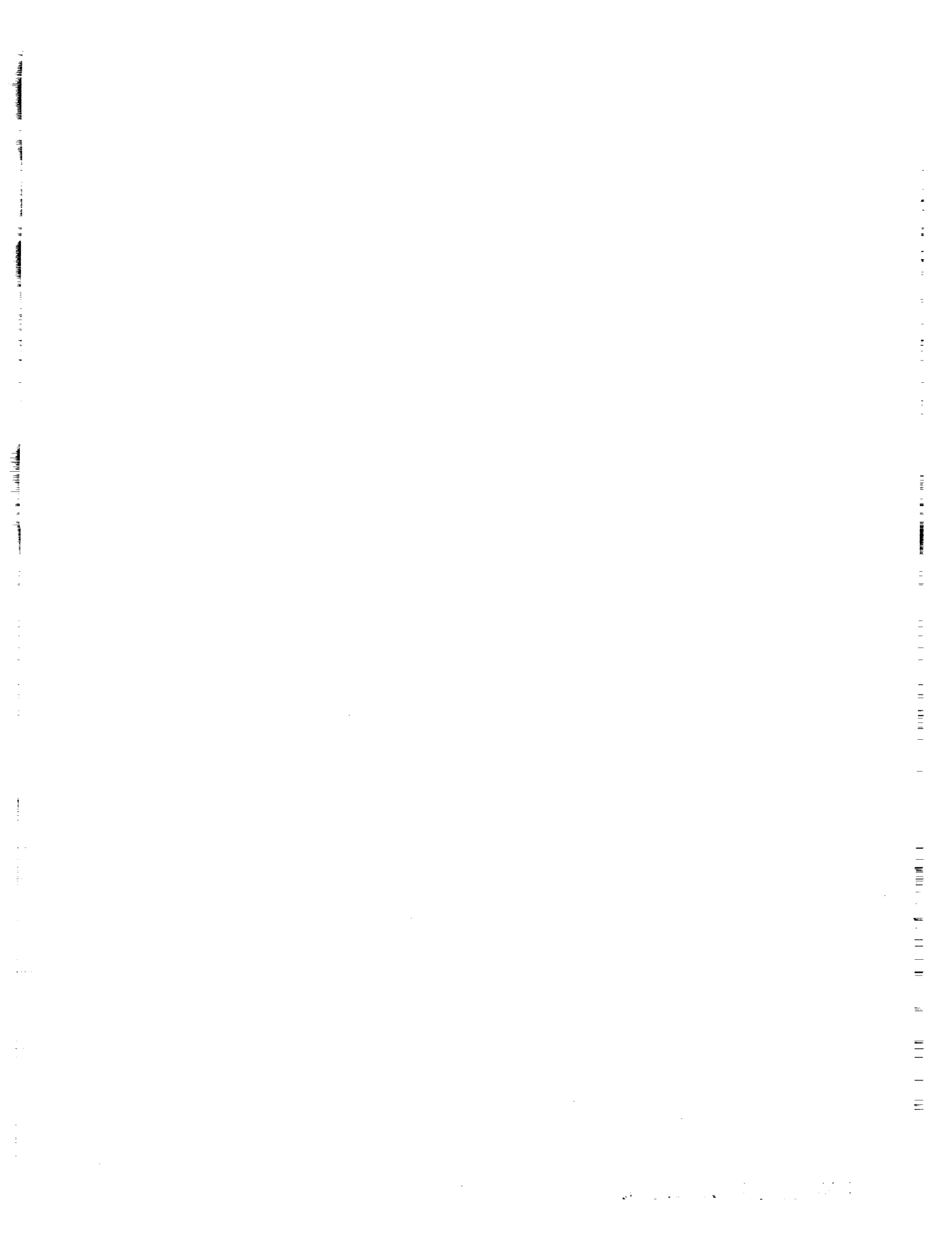
Figure 1	Annual mean ozone levels at Arosa, Switzerland, 1933–1982	763
Figure 2	Arosa data with least-squares fitted lines	763
Figure 3	Seasonal structure of monthly Arosa data	770



APPENDIX E

List of Tables

PRECEDING PAGE BLANK NOT FILMED



Appendix E

List of Tables

Table 2.1	SBUV r and s values	27
Table 2.2	Comparison of SBUV and TOMS r values for combined periods 1-2 ..	29
Table 2.3	Coefficients for the quasi-linear model	33
Table 2.4	Model values of diffuser D after 8 years	43
Table 2.5	Midlatitude ozone changes (1978-1986) for different diffuser degradation models	44
Table 2.6	Model values of diffuser D after 8 years	50
Table 2.7	Range of uncertainty in total ozone	52
Table 2.8	SAGE instrument characteristics	55
Table 2.9	Errors of SAGE-I and SAGE-II	61
Table 2.10	Errors in the difference between SAGE-I and SAGE-II	64
Table 2.11	Characteristics of LIMS channels	85
Table 2.12	Comparison of important features between SBUV-2 and SBUV	93
Table 3.1	Sensitivity of retrieved total ozone to diffuser plate reflectivity, $d \ln \Omega / d \ln D_A$, for TOMS at two view angles, θ , and for SBUV. The reference atmosphere contains 280 Dobson Units (DU) of ozone, surface reflectivity is 0.3, and the solar zenith angle is 45°	118
Table 3.2	Sensitivity of retrieved total ozone to Diffuser plate model error scenarios. The basic state is as for Table 3.1. The details of the scenarios are discussed in the text.	119
Table 3.3	Layer numbers used by SBUV and Umkehr retrievals	124
Table 3.4.	Effective ozone absorption coefficients for Dobson C-Pair	137
Table 3.5.	Averaging kernel peak heights and widths	140
Table 3.6	Summary of retrieval characteristics	175
Table 4.1	Ultraviolet wavelength pairs used for atmospheric ozone measurements with Dobson spectrophotometers (wavelengths in nanometers).	185
Table 4.2	Possible causes of error in ozone trends from Dobson stations; estimates of the effects on the determined trends due to instrumental and other experimental causes.	189
Table 4.3	Dobson stations for which preliminary revised ozone data are available over time periods long enough for trend analysis.	191
Table 4.4	Other Dobson stations for which the records are too short for trend analysis, have major interruptions in their records, or are otherwise unsuitable at the present time for analysis on an individual basis.	192
Table 4.5	Primary and secondary standard Dobson ozone spectrophotometers. .	194
Table 4.6	Summary of results of calibrations of world standard Dobson spectrophotometer No. 83 with standard lamps and by means of direct-Sun observations at Mauna Loa Observatory.	195
Table 4.7	USSR M-83 ozone stations.	199
Table 4.8	Six-month average bias (Dobson-TOMS)/Dobson centered at February 1 and August 1 of each year as deduced from all and from only direct-Sun observations.	209
Table 4.9	Stations with variability of their monthly mean differences with TOMS ≥ 3 percent.	213
Table 4.10	Provisionally revised station data used in the time series analyses.	230

TABLES

Table 4.11	Results of trend analyses of the monthly ozone values at Belsk, Poland, for the period 3/63–7/86.	232
Table 4.12	Changes in average total ozone concentrations as measured at individual Dobson stations over the 22-year period 1965–1986, inclusive.	243
Table 4.13	Parameter values for several linear ramp statistical calculations with ozone data from Bismarck.	248
Table 4.14	Statistical analyses of ozone data from Bismarck.	250
Table 4.15	Monthly means and standard deviations at Bismarck (in DU).	259
Table 4.16	Winter and summer trends for individual stations	262
Table 4.17	Average monthly ozone changes for different continents, 1970–1986	270
Table 4.18	Average monthly ozone changes for different continents, 1976–1986.	272
Table 4.19	Average monthly ozone changes, 1970–1986 (data for 1957–1986).	274
Table 4.20	Statistical evaluations of ozone depletion from atmospheric nuclear testing using data from individual stations	276
Table 4.21	Monthly trends in ozone when allowance is made for depletion by nuclear testing.	277
Table 4.22	Statistical evaluation of ozone variations in response to the solar sunspot cycle.	281
Table 4.23	Monthly coefficients (in DU/yr) for the three latitude bands for 1965–1986 data.	285
Table 4.24	Monthly coefficients (in DU/yr) for the same bands as in Table 4.23 for 1957–1986 data.	287
Table 4.25	Different ways of calculating an annual rate of loss.	290
Table 4.26	Variance and covariance of the monthly trend estimates used in calculating seasonal averages.	296
Table 4.27	Percentage changes in total column ozone (measured by TOMS on Nimbus-7, calibrated by comparison with ground-based measurements)	303
Table 5.1	Ozone measuring systems and periods of available data	387
Table 5.2	SAGE systematic errors	395
Table 5.3	SAGE errors affecting the precision and repeatability of ozone measurements for a vertical resolution of 1 km	395
Table 5.4	Comparison of important features between SBUV-2 and SBUV	411
Table 5.5	SBUV trend collocated with 11 Umkehr stations, the trend of the difference (SBUV–Umkehr), and the derived Umkehr trend for 1979 to 1986	417
Table 5.6	Corrections for aerosols applied to Umkehr data on the basis of lidar measurements and DeLuisi's model	419
Table 5.7	Linear least-squares ozone trends in Umkehr layers 6, 7, and 8 from January 1, 1979, to December 31, 1986	423
Table 5.8	Sensitivity study of the effect of three different assumed size distributions for aerosols: the distribution function based on observed aerosols and two widely different arbitrary distributions	424
Table 5.9	The beginning and ending dates (in 1979) and latitudes of four cases of longitudinal progression of the SAGE-I observations	427
Table 5.10	Estimated overall percentage differences of the calculated zonal mean ozone layer amount of SBUV, SAGE-I, and LIMS with respect to the average of these instruments	431
Table 5.11	Reproducibility of satellite and rocket systems in measuring upper stratospheric ozone near Natal, Brazil, during periods of atmospheric stability in 1979 and 1985	438
Table 5.12	Replication of upper stratospheric ozone by sets of three instruments	439

TABLES

Table 6.1	Sensitivity of measured SSU brightness temperatures to 8 ppmv CO ₂ increase and 10 percent ozone decrease at all levels	454
Table 6.2	Global daily 1200 GMT temperature and height fields history of changes	455
Table 6.3	Rocketsonde launch sites having data available for trend analysis	458
Table 6.4	Example of arcasonde and datasonde measurements of same temperature profiles and appropriate corrections	459
Table 6.5	100–50 mb layer mean temperature changes 1986/1985–1980/1979	472
Table 6.6	100–30 mb layer mean temperature changes 1986/1985–1980/1979	472
Table 6.7	30–10 mb layer mean temperature changes 1986/1985–1980/1979	473
Table 6.8	10–5 mb layer mean temperature changes 1986/1985–1980/1979	473
Table 6.9	5–1 mb layer mean temperature changes 1986/1985–1980/1979	474
Table 6.10	0.5 mb layer mean temperature changes 1986/1985–1979/1980	474
Table 6.11	Radiative transfer models used in this section	486
Table 6.12	Dependence of radiative convective equilibrium temperatures on cloud properties	493
Table 6.13	Comparison of calculated cooling from one-dimensional radiative–photochemical models near to the level of peak cooling	496
Table 6.14	Comparison of calculated cooling from one-dimensional radiative–photochemical models at about 30 mb (24 km)	497
Table 7.1	Factors included in model simulations	504
Table 7.2	Trace gas scenarios adopted for 1950–1991	504
Table 7.3	Fluorocarbon emission fluxes (10 ⁹ g/yr) used in models for 1950–1991	505
Table 7.4	Assumed peak-to-peak variation of UV radiation during a solar cycle as a function of wavelength	506
Table 7.5	Relative magnitude of solar cycles	507
Table 7.6	Limited set of nuclear tests used in model calculations	508
Table 7.7	Characteristics of 2-D models used in calculations of Chapter Seven	509–510
Table 7.8	Total chlorine mixing ratio (Cl _y in ppb) in the upper stratosphere at 30°N for July	520
Table 7.9	Calculated temperature changes in 1985 vs. 1979 for Oslo model, Case 3. Values are given for July at the equator	521
Table 7.10	Calculated trends in ozone at Umkehr levels 5–9 for 1970–1981; trace gas scenario only	534
Table 8.1	Updated global trends and tropospheric concentrations of source gases for 1986. Where appropriate and available, lifetimes are also tabulated.	547
Table 8.2	Annual mean halocarbon concentrations (pptv) observed at the GAGE sites in 1985. the data must be regarded as preliminary. The global average is the mean of the four GAGE sites. CCl ₃ F data were collected on a porosil column.	548
Table 8.3	Halocarbon growth rates (pptv/yr) observed at the ALE–GAGE sites over the period 1978 to June 1986. the data must be regarded as preliminary. Adrigole ceased operation in 1984. Growth rates were obtained by least squares linear regression; the numbers in parentheses are single standard deviations. The global average is the mean of growth rates observed at Oregon, Barbados, Samoa, and Cape Grim. CCl ₃ F data are from the porosil column.	548
Table 8.4	Halocarbon growth rates (%/yr) observed at the GAGE sites in 1985. Data are obtained from Tables 8.1 and 8.2.	553

TABLES

Table 8.5	Annual mean halocarbon concentrations and trends observed at (a) Hokkaido, Japan (42° to 45°N) (Makide et al., 1987a), and (b) Oregon, USA (45°N) (GAGE data), in 1985. Concentrations are in pptv, annual increases (pptv/yr) were obtained by linear regression, and the number in parentheses is one standard deviation. Data at both sites were collected from 1979 to 1986.	554
Table 8.6	Annual mean CCl ₃ F and CCl ₂ F ₂ concentrations (pptv) and increases (pptv/yr, %/yr) observed at the five Geophysical Monitoring for climatic change stations.	555
Table 8.7	Comparison of growth rates of atmospheric methane. For all data sets except UC the growth rates are given by the slope of a least squares linear fit to 12-month running mean methane values calculated from the monthly data. The values in parentheses are the standard errors of these slopes. The growth rate for the UC data was found by a least squares linear fit to the actual data over the period specified.	564
Table 10.1	Properties of atmospheric aerosols and clouds	600
Table 10.2	Time constants for aerosol processes	608
Table 10.3	Sites of long-term aerosol lidar observations	611
Table 10.4	Long-term aerosol measurements from satellites	616
Table 10.5	Observational methods used to study the stratospheric effects of the El Chichón volcanic eruption	624–625
Table 10.6	Volcanic eruptions known to have injected material into the stratosphere	630
Table 10.7	Aerosol impact on Umkehr and SBUV measurement systems, in order of importance of aerosol properties to each system	636
Table 10.8	Observed PSC properties: 1979 to 1981	644
Table 11.1	Zonal mean, minimum, and maximum ozone for the month of October each year for the 70°S–80°S latitude zone from Nimbus-4 BUV (1970–1972) and from Nimbus-7 SBUV (1979–1984).	671
Table 11.2	TOMS total ozone monthly zonal average	676
Table 11.3	Heterogeneous reactions in PSC's	732
Table 11.4	Observed vertical column abundance (mol. cm ⁻²)	740

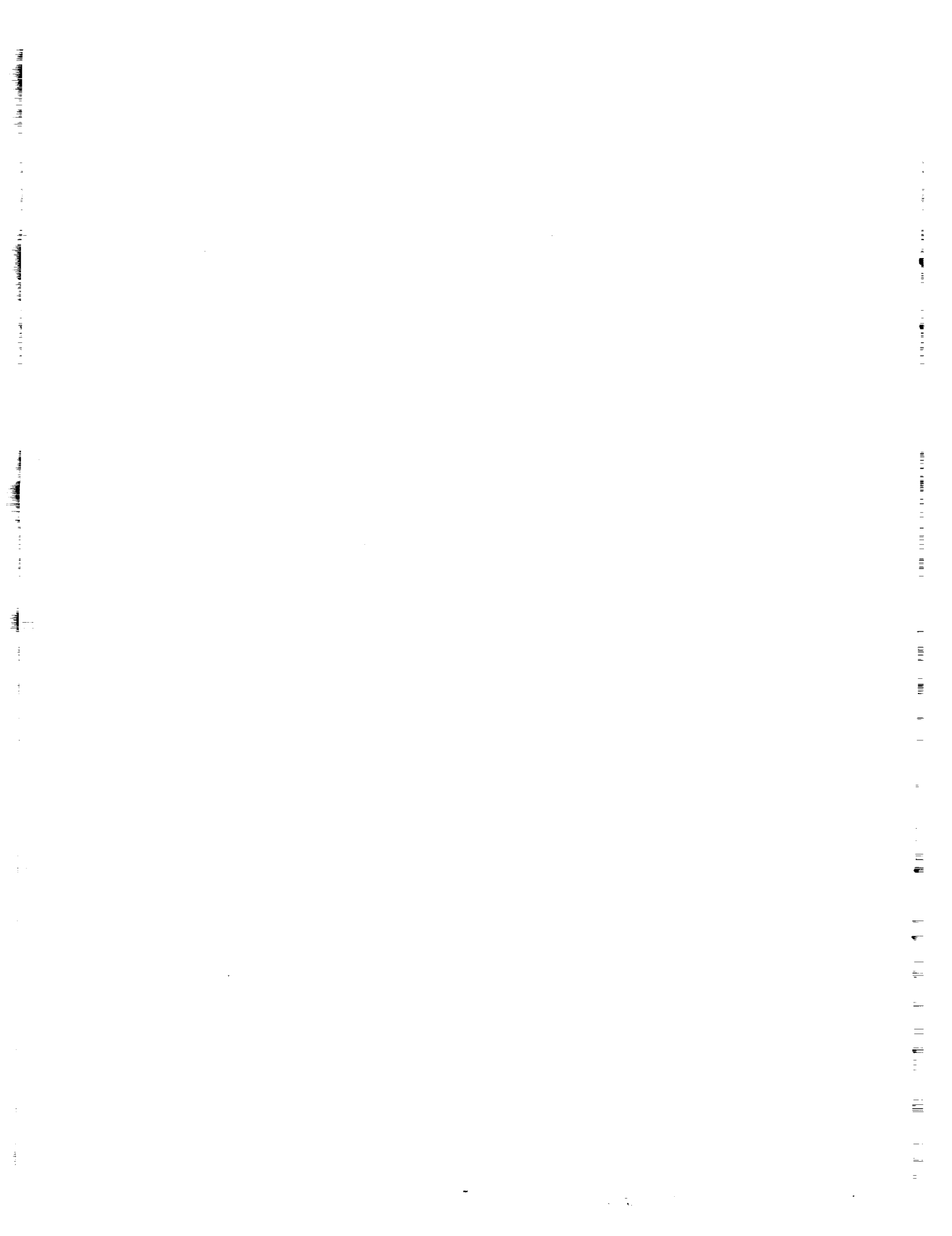
Appendix

Table 1	Dobson networks used in total ozone trend analysis	757
Table 2	Coefficients of least-squares lines	762

APPENDIX F

Major Acronyms

PRECEDING PAGE BLANK NOT FILMED



Appendix F

Major Acronyms

AER, Inc.	Atmospheric and Environmental Research, Incorporated
AERE	Atomic Energy Research Establishment (UK)
AFCRL	Air Force Cambridge Research Laboratories
AFGL	Air Force Geophysical Laboratory
AGU	American Geophysical Union
AIAA	American Institute of Aeronautics and Astronautics, Inc.
NOAA/AL	Aeronomy Laboratory
ARC	Ames Research Center (NASA)
ATMOS	Atmospheric Trace Molecule Spectroscopy Experiment
AVHRR	Advanced Very High Resolution Radiometer
BOIC	Balloon Ozone Intercomparison Campaign
BUV	Backscatter Ultraviolet Spectrometer
CFC	Chlorofluorocarbon
CFM	Chlorofluoromethane
CIMO	Commission on Instrument and Method of Observation
CIRA	COSPAR International Reference Atmosphere
CMA	Chemical Manufacturers Association
CMRN	Cooperative Meteorological Rocketsonde Network
CNRS	Centre National de la Recherche Scientifique (France)
COSPAR	Committee on Space Research
CPOZ	Compressed Profile Ozone
CSIRO	Commonwealth Scientific and Industrial Research Organization
DCA	Detector capsule assembly
DU	Dobson Unit
ECC	Electrochemical cell (ozonesonde)
EGA	Emissivity growth approximation
EMR	Electromagnetic radiation
ENSO	El Niño-Southern Oscillation
EOS	Earth Observing System
ERBS	Earth Radiation Budget Satellite
ERL	Environmental Research Laboratory (NOAA)
FGGE	First GARP Global Experiment
FOV	Field of view
FRG	Federal Republic of Germany
GARP	Global Atmospheric Research Program
GDR	German Democratic Republic
GFDL	Geophysical Fluid Dynamics Laboratory
GHRS	Goddard High Resolution Spectrograph

ACRONYMS

GMCC	Geophysical Monitoring for Global Change (NOAA)
GMT	Greenwich Mean Time
GSFC	Goddard Space Flight Center (NASA)
HIRS	High Resolution Infrared Radiation Sounder
hPa	hectoPascals
IAGA/IAMAP	International Association for Geomagnetism and Aeronomy/International Association for Meteorology and Atmospheric Physics
ICSU	International Council of Scientific Unions
IFC	Inflight calibrator
IFOV	Instrument field of view
IGY	International Geophysical Year
INPE	Brazilian space agency
IOC	International Ozone Commission
IPV	Isentropic potential vorticity
IR	Infrared
JPL	Jet Propulsion Laboratory
LAMAT	LIMS Map Archival Tapes
LaRC	Langley Research Center (NASA)
LASP	Laboratory for Atmospheric and Space Physics (University of Colorado)
LIMS	Limb Infrared Monitor of the Stratosphere
LLNL	Lawrence Livermore National Laboratory
LRIR	Limb Radiance Inversion Radiometer
LTE	Local Thermodynamic Equilibrium
MAP	Middle Atmosphere Program
MSU	Microwave Sounding Unit
NASA	National Aeronautics and Space Administration
NBS	National Bureau of Standards (now NIST)
NCAR	National Center for Atmospheric Research
NDSC	Network for the Detection of Stratospheric Change
NESDIS	National Environmental Satellite Data and Information Service
NIR	Near infrared
NMC	National Meteorological Center
NMHC	Nonmethane hydrocarbons
NOAA	National Oceanic and Atmospheric Administration
NOZE	National Ozone Expedition
NRC	National Research Council
NRL	Naval Research Laboratory
NSSDC	National Space Science Data Center
ODW	Ozone Data for the World
OGO	Orbiting Geophysical Observatory
OPT	Ozone Processing Team
PMR	Pressure Modulated Radiometer
PMT	Photomultiplier tube
PSC	Polar Stratospheric Cloud
QBO	Quasi-Biennial Oscillation

ACRONYMS

RAOB	Rawinsonde Observation
ROCOZ	Rocket Ozonesonde
SAGE	Stratospheric Aerosol and Gas Experiment
SAM-II	Stratospheric Aerosol Measurement
SAMS	Stratospheric and Mesospheric Sounder
SAO	Smithsonian Astrophysical Observatory (Cambridge, MA)
SBUV	Solar Backscatter Ultraviolet Spectrometer
SCOSTEP	Scientific Committee on Solar Terrestrial Physics
SCR	Selective Chopper Radiometer
SIRIS	Stratospheric InfraRed Interferometer Spectrometer
SME	Solar Mesosphere Explorer
SMM	Solar Maximum Mission
SPIE	International Society for Optical Engineering
SSU	Stratospheric Sounding Unit
THIR	Temperature Humidity Infrared Radiometer
TIROS	Television and Infrared Observation Satellite
TOMS	Total Ozone Mapping Spectrometer
TOVS	TIROS Operational Vertical Sounder
UARS	Upper Atmosphere Research Satellite
UKMO	United Kingdom Meteorological Office
UNEP	United Nations Environment Program
UVS	Ultraviolet Spectrometer
UVSP	Ultraviolet Spectrometer and Polarimeter
VTPR	Vertical Temperature Profile Radiometer
WMO	World Meteorological Organization
WODC	World Ozone Data Center



APPENDIX G

Chemical Formulae and Nomenclature

PRECEDING PAGE BLANK NOT FILMED

Appendix G

Chemical Formulae and Nomenclature

Symbol	Name	Symbol	Name
O	Atomic oxygen	CH ₂ O	Formaldehyde
O ₂	Molecular oxygen	CH ₃ CHO	Acetaldehyde
O ₃	Ozone	(CH ₃) ₂ CO	Acetone
O _x	Odd oxygen (O, O(¹ D), O ₃)	CH ₃ O ₂ H	Methyl hydroperoxide
N ₂	Molecular nitrogen	CH ₂ CHCHO	Acrolein
N ₂ O	Nitrous oxide	C ₂ Cl ₄	Tetrachloroethylene
NO	Nitric oxide	CH ₃ Cl	Methyl chloride
NO ₂	Nitrogen dioxide	CH ₂ Cl ₂	Dichloromethane
NO ₃	Nitrogen trioxide, nitrate radical	CHCl ₃	Chloroform, trichloromethane
NO _y	Odd nitrogen (NO, NO ₂ , NO ₃ , N ₂ O ₅ , ClONO ₂ , HNO ₄ , HNO ₃)	CFC	Chlorofluorocarbon
NO _x	Oxides of nitrogen (NO, NO ₂ , NO ₃)	HC	Hydrocarbon
N ₂ O ₅	Dinitrogen pentoxide	NMHC	Nonmethane hydrocarbons
HNO ₂ , HONO	Nitrous acid	PAN	Peroxyacetylnitrate
HNO ₃ , HONO ₂	Nitric acid	CH ₃ CCl ₃	Methyl chloroform
HNO ₄ , HO ₂ NO ₂	Peroxyntiric acid	C ₂ F ₆	Hexafluoroethane
NH ₃	Ammonia	CCl ₄	Carbon tetrachloride (FC-10)
H ₂ O	Water vapor	CCl ₃ F	Trichlorofluoromethane (FC-11)
H ₂ O ₂	Hydrogen peroxide	CCl ₂ F ₂	Dichlorodifluoromethane (FC-12)
OH, HO	Hydroxyl radical	CClF ₃	Chlorotrifluoromethane (FC-13)
HO ₂	Hydroperoxyl radical	CF ₄	Tetrafluoromethane (FC-14)
HO _x	Odd hydrogen (OH, HO ₂ , H ₂ O ₂)	CHCl ₂ F	Dichlorofluoromethane (FC-21)
CO	Carbon monoxide	CHClF ₂	Chlorodifluoromethane (FC-22)
CO ₂	Carbon dioxide	CCl ₂ FCClF ₂	Trichlorotrifluoroethane (FC-113)
CS ₂	Carbon disulfide	CClF ₂ CClF ₂	Dichlorotetrafluoroethane (FC-114)
COS, OCS	Carbonyl sulfide	CClF ₂ CF ₃	Chloropentafluoroethane (FC-115)
SO ₂	Sulfur dioxide	CF ₃ CF ₃	Hexafluoroethane (FC-116)
SF ₆	Sulfur hexafluoride	CH ₃ CN	Methyl cyanide
H ₂ SO ₄	Sulfuric acid	CH ₃ I	Methyl iodide
HF	Hydrogen fluoride	Br	Bromine atom
HCl	Hydrogen chloride	BrO	Bromine monoxide
HCN	Hydrogen cyanide	Br _x	Odd bromine, inorganic bromine
HOCl	Hypochlorous acid	CBrF ₃	Trifluorobromomethane
Cl	Chlorine atom	CHBr ₃	Bromoform, tribromomethane
ClO	Chlorine monoxide	CH ₃ Br	Methyl bromide
ClONO ₂ , ClNO ₃	Chlorine nitrate	CH ₂ Br ₂	Dibromomethane
Cl _x	Odd chlorine, inorganic chlorine	CHBr ₂ Cl	Dibromochloromethane
CH ₄	Methane	C ₂ H ₄ Br ₂	Dibromoethane
C ₂ H ₆	Ethane	CBrClF ₂	Halon 1211 (BCF) FC-12B1
C ₃ H ₈	Propane	CF ₃ Br	Halon 1301 FC-13B1
C ₂ H ₄	Ethylene		
C ₂ H ₂	Acetylene		



APPENDIX H

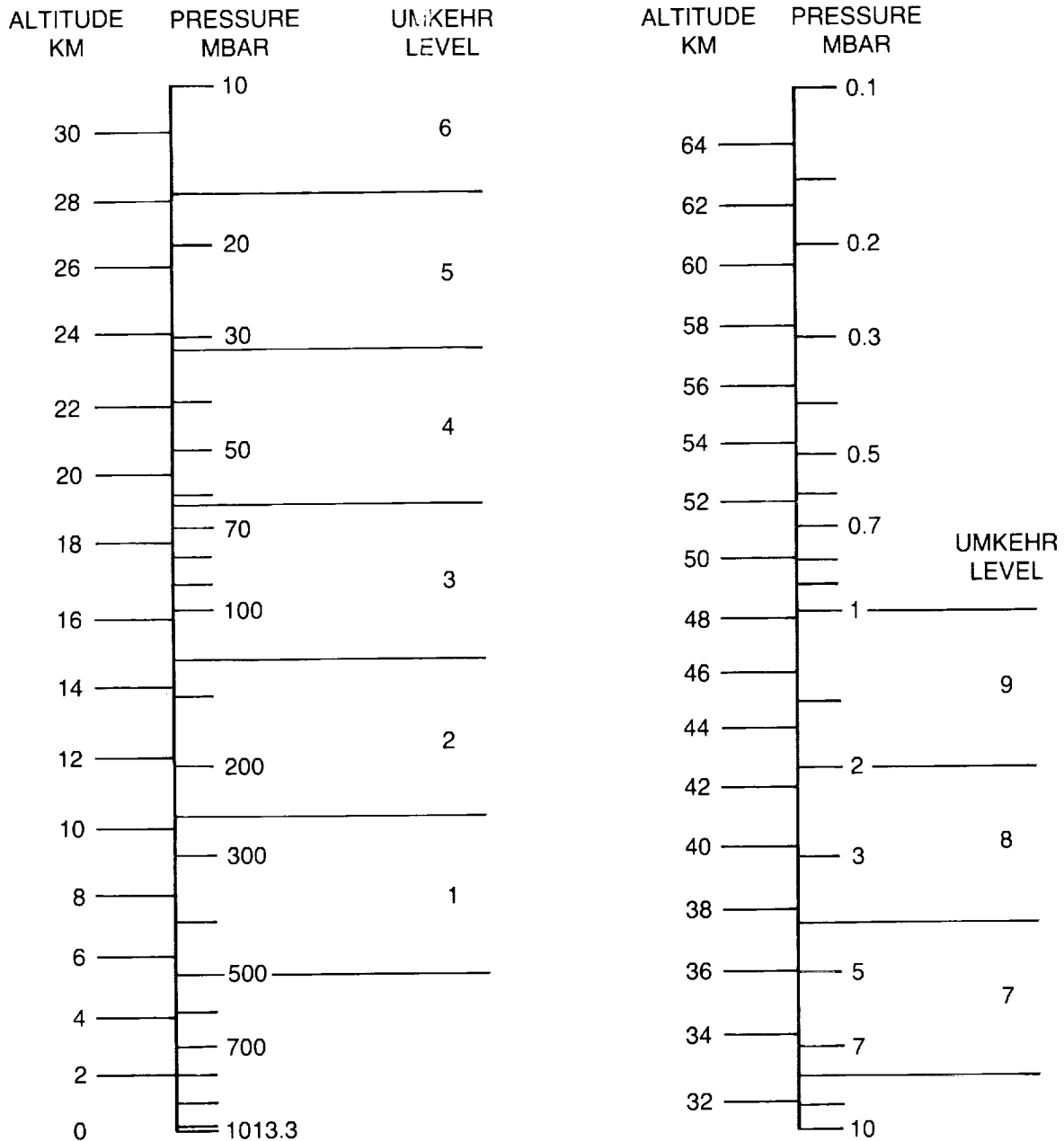
Pressure—Altitude Conversion Chart

PRECEDING PAGE BLANK NOT FILMED

Appendix H

Pressure-Altitude Conversion Chart

PRESSURE-ALTITUDE



Altitudes are based on U.S. Standard Atmosphere, 1976. The actual altitude for a given pressure may differ by as much as 2 km, depending on season, latitude, and short-term variations.

